10 Maximum-Likelihood Estimation in Experimental Quantum Physics

Gerald Badurek[1], Zdeněk Hradil[2], Alexander Lvovsky[3], Gabriel Molina-Teriza[4], Helmut Rauch[1], Jaroslav Řeháček[2], Alipasha Vaziri[4], and Michael Zawisky[1]

[1] Atominstitut der Österreichischen Universitäten, Stadionallee 2, 1020 Wien, Austria, rauch@ati.ac.at
[2] Department of Optics, Palacky University, 17. listopadu 50, 772 00 Olomouc, Czech Republic, hradil@aix.upol.cz
[3] Universität Konstanz, Fakultät für Physik, Fach 696, 78457 Konstanz, Germany, www.uni-konstanz.de/quantum-optics/quantech/
[4] Institut für Experimentalphysik, Universität Wien, Boltzmanngasse 5, 1090 Wien, Austria

Abstract. The theory of quantum state reconstruction is illustrated here on several examples taken from modern experimental praxis. Maximum-likelihood estimation is applied to experiments on physical systems of increasing complexity, starting with a simple one-dimensional problem of quantum phase estimation, continuing with the absorption and phase neutron tomographies, further discussing quantum tomography of higher-dimensional discrete quantum systems, and closing with the homodyne tomography of an infinite dimensional system - a mode of light. All these experiments nicely demonstrate the utility of present state-of-art techniques for manipulating states of a neutron and internal as well as external states of a photon.

10.1 Introduction

Over the past hundred years, quantum theory proved to be an extremely useful tool for describing and understanding nature on a microscopic level. Its usual applications consist in predicting the outcomes of future experimental results given a quantum state describing the physical system.

However, in experimental physics one often faces a different question: "Given the outcomes of a particular set of measurements, what quantum state do they imply?" Such *inverse problems* may arise for instance in the stage of setting up and calibrating laboratory sources of quantum states, in the analysis of decoherence and other deteriorating effects of the environment, or in some special tasks in quantum information processing such as eavesdropping on a quantum channel in quantum cryptography.

Quantum state reconstruction is a highly nontrivial problem. The quantum state of a system, however simple, cannot be determined by a single measurement. Repeated identical measurements performed on multiple identical copies of a quantum state generally will not yield the complete information about the ensemble in question. Such a set of measurements will,

G. Badurek et al., Maximum-Likelihood Estimation in Experimental Quantum Physics, Lect. Notes Phys. **649**, 373–414 (2004)
http://www.springerlink.com/

however, provide the probability distribution of the ensemble measured over the eigenstates of the measurement apparatus.

To fully characterize an ensemble one needs to perform a set of multiple, *different* measurements on an even larger set of the identically prepared systems. By modifying the configuration of the apparatus, one acquires the quantum state statistics associated with various measurement bases. A set of these distributions contains complete information about the system, which can be then extracted in the form of a density matrix. In a sense, many different and mutually incompatible observations are compressed to a single mathematical object.

Various theoretical approaches to this problem are reviewed in other chapters in this volume. The purpose of this chapter is to provide the reader with some examples of quantum tomography taken from the modern experimental praxis. Maximum likelihood estimation will be applied to physical systems of increasing complexity starting with a simple one-dimensional problem of quantum phase, continuing through the absorption and phase neutron tomographies, further discussing quantum tomography of discrete quantum systems, and closing with the homodyne tomography of an infinite dimensional system—a mode of light.

10.2 Maximum-Likelihood Phase Estimation

Phase measurements do not belong to the category of conventional measurements since a Hermitian phase operator does not exist in the canonical sense [1–5]. However, this does not mean that phase cannot be described in quantum theory or even measured. Let us first briefly review some basic facts related to experimental reality.

From the point of view of estimation theory [6] phase is a c-number parameter appearing in the transformation describing the action of a phase shifter on the input state $|\Psi\rangle$

$$|\Psi(\bar{\theta})\rangle = e^{-i\bar{\theta}\hat{N}}|\Psi\rangle, \tag{10.1}$$

$\hat{N} = \hat{a}^\dagger\hat{a}$ being the photon-number operator. Any phase measurement is completely described by the statistics $p(\theta|\bar{\theta})$ of its outcomes θ conditioned on the true value $\bar{\theta}$ of the phase shift. Basically, two strategies may arise. One can either look for the *ideal measurement* [7–11], i.e. the measurement optimal from some point of view, or, provided that a measurement cannot be chosen at our will, one should choose the statistical data analysis extracting as much information about the parameter of interest as possible.

The statistics of the ideal phase measurement are just the statistics of the Susskind-Glogower phase operator [12],

$$p(\theta|\bar{\theta}) = \frac{1}{2\pi}|\langle\theta|\Psi(\bar{\theta})\rangle|^2, \quad \hat{a}\hat{N}^{-1/2}|\theta\rangle = e^{i\theta}|\theta\rangle. \tag{10.2}$$

Although the eigenstates of this operator are not orthogonal, they are overcomplete, and thus generate probability operator valued measure (POVM) $\Pi(\theta) = |\theta\rangle\langle\theta|$, that defines the ideal phase measurement in the sense of generalized measurements.

Though there are ways to simulate measurement (10.2) by means of post selection [13], this does not seem to be a practical solution. What is usually measured in practice is energy, and phase sensitive devices called interferometers are used to transform phase shifts into variations of output energies. Due to the statistical nature of quantum theory, the resulting relationship between the measured quantities and the parameters of interest is not deterministic. Such an indirect inference is usually called quantum estimation, and its scheme is the following:

$$\rho \to \boxed{\begin{array}{l}\text{true phase}\\ \text{shift}\quad \bar{\theta}\end{array}} \to \rho(\bar{\theta}) \to \boxed{\text{detection}} \to \mathbf{n}(\bar{\theta}) \to \boxed{\text{estimation}} \to \theta(\mathbf{n}).$$

An interferometer provides the input-output transformation of the known initial state ρ. The subsequent measurement yields a phase sensitive data $\mathbf{n}$ that are processed to get a phase estimate θ. The true phase shift $\bar{\theta}$ inside the interferometer, which is a non-fluctuating parameter controlled by the experimentalist, should carefully be distinguished from the phase estimate θ, which is generally a random quantity.

The performance of the estimation of course depends on the choice of the estimator. The point estimators of phase corresponding to the ML estimation will be used here [8,14]. In accordance with the ML approach [15], the sought-after phase shift is given by the value, which maximizes the likelihood function

$$\mathcal{L} \equiv p(\theta|\mathbf{n}) \propto p(\mathbf{n}|\theta). \tag{10.3}$$

A schematic representation of a Mach-Zehnder (MZ) interferometer is shown in Fig. 10.1. Its input ports are fed by n_1 and n_2 particles. Formally, this device can be described by Lie algebra SU(2), the correspondence being provided by the Schwinger representation of the angular momentum operators.

The phase resolution of the MZ interferometer strongly depends on the properties of the input signal. Provided that the interferometer is operated in the usual (classical) manner with the light entering one input port only, $|\text{in}\rangle = |N, 0\rangle$, the phase error is proportional to $1/\sqrt{N}$. This regime is usually referred to as the standard limit of phase measurements. When both the input ports of the interferometer are fed by the signal with an equal number of particles, $|\text{in}\rangle = |N/2, N/2\rangle$, the theory predicts the ultimate phase resolution of $\Delta\theta \approx 1/N$, which is the quantum limit of phase measurements [9, 10].

While the classical limit can be achieved using a coherent source, or by accumulating data from repeated single particle interference experiments, the quantum limit requires a bright source of highly nonclassical exotic states such as Fock states or highly squeezed states [7, 9], which are still not readily available in laboratories. But even in the absence of such resources one

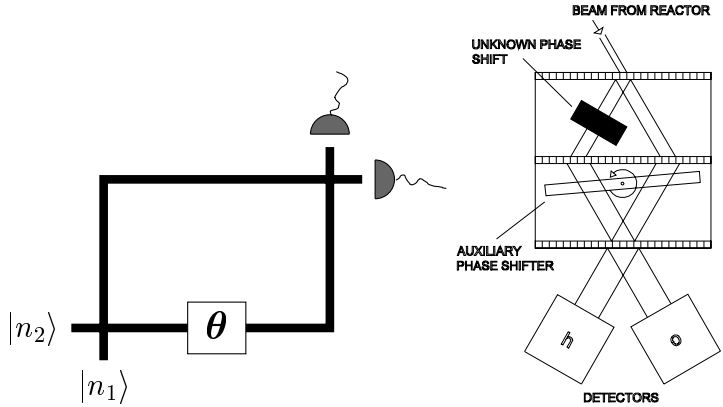

Fig. 10.1. Left side: Mach-Zehnder optical interforemeter; right side: silicon perfect crystal interferometer used in neutron optics.

can still benefit from the proper data manipulation as will be shown on the example of a semi-classical and fully quantum phase reconstruction.

The quantum phase reconstruction can also be regarded as the simplest case of a quantum-state reconstruction. A single particle being in a superposition of two paths is equivalent to a two-level system and can therefore be visualized by a point inside the Bloch sphere. The action of the interferometer is related to the equatorial cut through this sphere: The phase shift rotates the Bloch vector along the equator, while the decoherence affecting the visibility contracts this vector. So the natural parameter space of the phase reconstruction is a unit circle.

10.2.1 Quantum Phase Estimation

First, let us show that the operational phase concepts can naturally be embedded in the general scheme of quantum estimation theory [6, 16] as was done in [17–20].

Let us consider a MZ interferometer, where the measurement is performed with zero and $\pi/2$ auxiliary phase shifters. The auxiliary shifter is needed to get a unique phase estimate. Such a device is equivalent to the 8-port homodyne detection scheme [21] with the four output channels numbered by indices 3,4,5, and 6, where the numbers of particles are registered in each run. Assume that the these quantities fluctuate in accordance with some statistics. The mean intensities are modulated by a phase parameter $\bar{\theta}$

$$\bar{n}_{3,4} = \frac{N}{2}(1 \pm V\cos\bar{\theta}), \quad \bar{n}_{5,6} = \frac{N}{2}(1 \pm V\sin\bar{\theta}), \tag{10.4}$$

where N is the total intensity and V is the visibility of the interference fringes. Provided that a particular combination of outputs $\{n_3, n_4, n_5, n_6\}$ has been registered, the phase shift can be inferred.

Now, for a while, let us assume that the phase sensitive device operates with a Gaussian signal with phase insensitive noise. This is only an approximation to the real situation since realistic signals are discrete. Under such approximation, the likelihood function corresponding to the detection of given data reads

$$\mathcal{L} \propto \exp\Big\{-\frac{1}{2\sigma^2}\sum_{i=3}^{6}[n_i-\bar{n}_i]^2\Big\}. \tag{10.5}$$

Here the variance σ^2 represents the phase insensitive noise of each channel. The sampling of intensities may serve for the estimation of the phase shift and visibility simultaneously. Likelihood function (10.5) is maximized on the physically allowed space of parameters $V \leq 1$ by the following phase and visibility,

$$e^{i\theta} = \frac{n_3 - n_4 + i(n_5 - n_6)}{\sqrt{(n_3-n_4)^2+(n_5-n_6)^2}}, \tag{10.6}$$

$$V = \min\left(2\frac{\sqrt{(n_3-n_4)^2+(n_5-n_6)^2}}{\sum_{i=3}^{6} n_i}, 1\right). \tag{10.7}$$

Notice that the prediction of this semi-classical theory (10.6) coincides with the operational quantum phase introduced by Noh, Fougères and Mandel (NFM) [22]. This means that operational phase concepts can be thought of as special cases of ML phase estimation – ML estimation for Gaussian signals. Such predictions are optimal only for signals represented by a continuous Gaussian signal with phase independent and symmetrical noises. Let us note that a generalization of this concept to a larger number of auxiliary phase shifts detected [23] is known as the phase of the discrete Fourier transformation.

Since realistic signals are discrete, the theory can be refined by considering the actual statistics of the experiment. This can be demonstrated on the case of Poissonian signals. These are frequently encountered in laboratories as ideal lasers, or thermal sources of particles, such as neutron beams. ML estimation based on the Poissonian likelihood function,

$$\mathcal{L} \propto \prod_{i=3}^{6} \frac{\bar{n}_i^{n_i}}{n_i!} e^{-\bar{n}_i}, \tag{10.8}$$

gives optimum values for the phase shift and visibility

$$e^{i\theta} = \frac{1}{V}\left[\frac{n_4-n_3}{n_4+n_3} + i\frac{n_6-n_5}{n_6+n_5}\right], \tag{10.9}$$

$$V = \sqrt{\left(\frac{n_4-n_3}{n_4+n_3}\right)^2 + \left(\frac{n_6-n_5}{n_6+n_5}\right)^2} \leq 1, \tag{10.10}$$

provided that the estimated visibility (10.10) is smaller than unity. If not, it is necessary to maximize the likelihood function (10.8) numerically on the boundary ($V = 1$) of the physically allowed region of parameters.

Relations (10.9-10.10) provide a correction of the semiclassical Gaussian theory with respect to the discrete Poissonian signals. The principle of inference together with the two different assumptions about the nature of the signal have given rise to two different phase estimates (10.6) and (10.9). One may wonder, whether the improvement of phase inference gained by taking the correct statistics of the experiment into account is worth giving up the simple NFM formalism and resorting to numerical methods. Could the optimization of the information yield from the measured data lead to a significant increase of the accuracy of the phase fitting?

The difference between recipes (10.6) and (10.9) can be tested in a controlled phase measurement. The phase difference is adjusted to a certain value and estimated independently using both the methods (10.6) and (10.9) in repeated experiments. The efficiency of both methods can then be compared.

Of course, some measure of the estimation error is needed for this. Dispersion defined by the relation

$$\sigma^2 = 1 - \left|\langle \mathrm{e}^{i\theta}\rangle\right|^2 \tag{10.11}$$

is one such reasonable measure. Here, the average is taken over the posterior phase distribution of the corresponding phase estimator.

The evaluation of the average quadratic cost (10.11) is not the only way to compare the efficiencies of different estimation procedures. Another possibility is to use the rectangular cost function

$$C(\theta - \bar{\theta}) = \begin{cases} -1 & |\theta - \bar{\theta}| \leq \Delta\theta \\ 0 & |\theta - \bar{\theta}| > \Delta\theta \end{cases} . \tag{10.12}$$

The averaged rectangular cost $\langle C(\theta - \bar{\theta})\rangle$ measures how many times the estimate θ falls within the chosen window $\Delta\theta$ spanning around the true phase $\bar{\theta}$. The difference

$$\Delta E = \langle C(\theta - \bar{\theta})\rangle_{\mathrm{Gauss}} - \langle C(\theta - \bar{\theta})\rangle_{\mathrm{Poiss}} \tag{10.13}$$

then measures how much the Poissonian prediction is better than the Gaussian one. If this quantity is found to be positive, the ML estimation is better than its NFM counterpart.

Although the dispersion (10.11), and ΔE cannot be calculated explicitly for an arbitrary input intensity N, it is possible to analyze the limit cases [20]. Obviously, both the predictions (10.6) and (10.9) will coincide provided that there is almost no information available in the low intensity limit, $N \to 0$. Not so obvious is the fact that both predictions will also coincide in the high intensity limit, $N \gg 1$, provided the visibility is low $V \to 0$. To see this, let

Table 10.1. Asymptotic dispersions and overall quadratic costs of various phase estimators. ML' – unconstrained ML estimation; ML_1 – single-parameter ML estimation. For comparison, CRLB is also shown.

Estimator	σ^2	$\bar{C} \equiv \int \sigma^2 d\bar{\theta}$
NFM	$1/N$	$2\pi/N$
ML'	$\left(1+\cos^2 2\bar{\theta}\right)/2N$	$\frac{3}{2}\pi/N$
ML	$\approx \left(1+0.5\cos^2 2\bar{\theta}\right)/2N$	$\approx \frac{5}{4}\pi/N$
ML_1	$1/2N$	π/N
CRLB	$1/2N$	π/N

us compare the asymptotic dispersion of the NFM estimator,

$$\sigma_G^2 \approx \frac{1}{V^2} N^{-1} + O\left(\frac{1}{N^2}\right), \tag{10.14}$$

with the asymptotic expression for the (CRLB) on the dispersion of any estimator,

$$\sigma_{CRLB}^2 = \frac{V^2 - 1 - \frac{1}{4}V^4 \sin^2 2\bar{\theta}}{V^2 - 1 - \frac{1}{2}V^2 \sin^2 2\bar{\theta}} V^{-2} N^{-1} + O\left(\frac{1}{N^2}\right). \tag{10.15}$$

If the visibility is low, both expressions will become identical. Therefore the semiclassical theory is optimal in this limit case [23].

Asymptotic expressions for various phase estimators in the opposite limit of high visibility $V \approx 1$ are given in Table 10.1. Estimator ML' is the phase prediction given by (10.9), that is, one does not care about the possible unphysical inferred visibilities $V > 1$, and ML_1 is the single-parameter estimation obtained by setting $V = 1$ in the likelihood function (10.8) and maximizing it only with respect to phase.

Notice that the uncertainties of all estimators scale as $1/\sqrt{N}$. This is to be expected in accordance with the standard quantum limit. However the constant of proportionality depends on the estimator used. By taking physical constraints into account the accuracy of phase fitting is improved.

The single-parameter ML_1 estimator is seen to provide best phase predictions. It attains the CRLB and hence is optimum. It yields a phase prediction whose uncertainty is reduced by the factor of $\sqrt{2}$, that is by about 30%, compared with the semi-classical theory. However, estimating phase alone implicitly presumes good a-priori knowledge of the visibility. If the actual value of the visibility is not known or fluctuates during the experiment, the single-parameter estimator may lead to biased phase predictions. For large intensities the bias might completely spoil the estimation [20].

10.2.2 Experiments

The performance of the semiclassical NFM and ML phase estimators have been determined in a series of experiments utilizing two principal sources

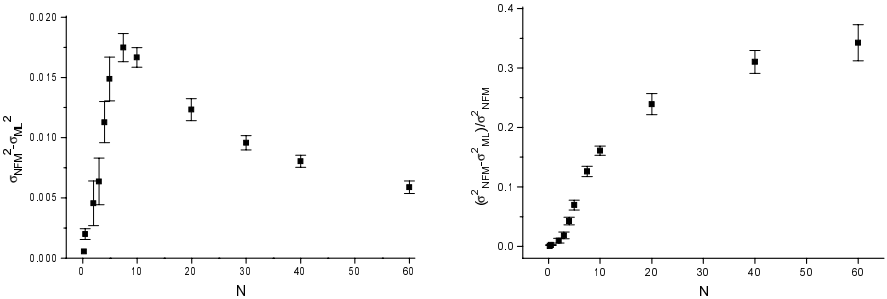

Fig. 10.2. The experimentally observed absolute (left panel) and relative (right panel) difference between the dispersions of the NFM and ML estimators as a function of the input mean number of photons N for fixed true phase $\bar{\theta} = \pi/3$. Error bars corresponding to 68% confidence intervals are also shown.

of particles – beams of thermal neutrons [19] and laser light [20]. The main goal of the experiments was to compare the optimum phase prediction with the semi-classical theory in the regime of only a few input particles. As a side result, the theoretical asymptotic uncertainties given in Table 10.1 were tested experimentally.

The dispersions (10.11) of the NFM (or equivalently Gaussian) and ML phase estimators found in experiments with light are shown in Fig. 10.2. The true phase was fixed at $\bar{\theta} = \pi/3$. The number of detected quadruples $\{n_3, n_4, n_5, n_6\}$ used for the calculation of the dispersions varied from 1000 samples for the input mean number of photons $N = 60$ to more than 100,000 samples for $N = 0.1$. The error bars corresponding to these finite numbers of samples are the result of numerical simulation. The visibility during the experiments was better than 99.6%.

The ML estimator was found to be significantly more accurate (by many standard deviations) than its NFM semi-classical counterpart. This was confirmed by evaluating the difference of the rectangular costs (10.13), see the left panel in Fig. 10.3. Here, the chosen input total energy roughly fits the maximum, $N \approx 7.5$, of the curve seen in Fig. 10.2.

A significant difference between the effectiveness of semi-classical and optimal treatments is apparent in Fig. 10.3. The optimal treatment provides an improvement in estimation procedure, and the difference is more than 10 standard deviations beyond the statistical error. High stability and visibility of interference fringes in the optical interferometer along with a high repetition rate of pulsed lasers made the improvement of the semi-classical phase prediction more evident than in a similar comparison that had been done with thermal neutrons [19], see the right panel in Fig. 10.3.

An experimental comparison of three different phase estimations – NFM, ML', and ML estimators – in the asymptotic regime is shown in Fig. 10.4. The experiment was done with photons. For comparison, the theoretical values of

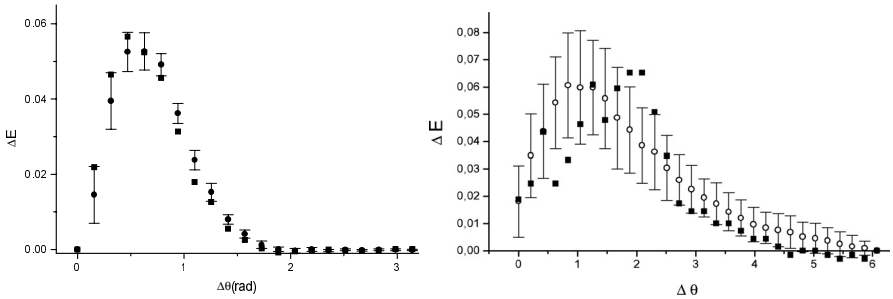

Fig. 10.3. Experimentally obtained ΔE (squares) compared to theoretical values (circles). Left panel: experiment with photons, $N = 10$ photons, visibility was better than 99.5%; error bars correspond to 7500 measured samples. Right panel: experiment with neutrons. The mean number of $N = 8.54$ incoming neutrons was asymmetrically split between the ordinary ($N_o = 2.21$) and extraordinary ($N_h = 6.33$) channels. The average visibility was about 31%; error bars correspond to 690 registered samples.

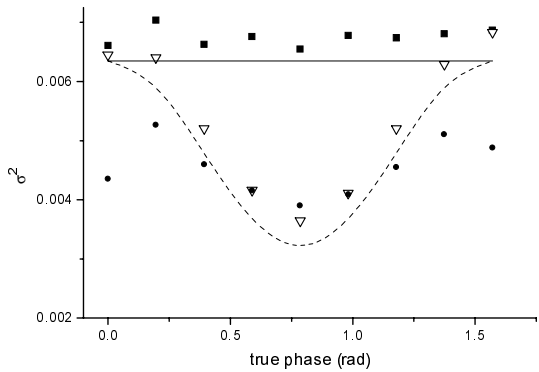

Fig. 10.4. Asymptotic dispersions of the semi-classical NFM estimator; theory (solid line) and experimentally obtained values (squares). Asymptotic dispersions of the unconstrained ML estimator; theory (dashed line) and experimentally obtained values (triangles). Experimentally obtained dispersions of the ML estimation on the physical space of parameters (circles). The corresponding input mean number of photons and the estimated visibility were $N = 160$ and $V = 99.2\%$, respectively.

dispersions given in Table 10.1 are also shown. Several important conclusions can be drawn from Fig. 10.4. (i) We can see that the uncertainty of the constrained ML estimation is definitely below the uncertainty of the unconstrained estimation in agreement with theory presented in Table 10.1. It means that insisting on the physical constraints (here the non-negativity of the intensity) is important not only for the sake of interpretation, but it also makes the estimation more efficient. Of course, both ML estimations beat the phase resolution of the semi-classical NFM theory. (ii) The observed val-

ues of dispersions exhibit a systematic error. The additional noise above the theoretical uncertainty is caused by inherent phase fluctuations in the experimental setup. Hence our statistically motivated evaluation of experimental data can be used for inferring the amount of fluctuations, and therefore it provides an independent and nontrivial way of calibrating an interferometer.

10.3 ML Neutron Absorption Tomography

Though the ML reconstruction has been proposed in quantum domain, it can be applied advantageously to any statistical theory, particularly to absorption tomography. This classical problem also illuminates the tomographic aspects of the quantum-state reconstruction.

The standard reconstruction method in present computerized tomographic (CT) imaging is the filtered back-projection (FBP) algorithm based on the inverse Radon transformation [24]. Technically, this transformation is implemented using fast Fourier transformation routines, which makes the reconstruction process fast and highly efficient. FBP gives satisfactory results in applications where (i) the intensity of the illuminating beam is so large that its statistics can safely be ignored, and (ii) the sample can be scanned over the whole 180° angular interval in small steps. In X-ray medical CT imaging these two conditions are usually met.

Unfortunately FBP fails in case of missing projections and/or if strong statistical fluctuations of the counting numbers are present in the small detector pixels. The latter situation occurs e.g. in neutron tomography [25–28], if monochromatic neutron beams are applied in order to avoid beam artifacts [29] or at the investigation of strong absorbing materials [30]. As present neutron sources are thermal in nature, they generate weak beams. Particles that have passed through the studied object are counted one by one and their statistical fluctuations have strong influence on the reconstructed images.

The case of missing projections or incomplete data sets is another important issue. If technical problems arise during the tomographic scan, FBP algorithm requires repeating the whole measurement. Partial or incomplete data cannot be inverted using this method. Sometimes it may be required to keep the sample in a cryostat during the measurement. The construction of such a cryostat may not allow turning it upside-down, so part of the measured angles may be missing, or there may not be enough space to rotate the sample in the full 180° interval. This was investigated in the past in detail by means of algebraic reconstruction techniques [31–33].

The maximum-likelihood reconstruction method described in this section can improve several tomographic applications in neutron optics which in many cases are limited by the weak intensity and the poor detector resolution [34,35]. Generally, it achieves better reconstruction results or reduce the scanning time in neutron optics and in medical and biological CT imaging.

In the following we will focus on the absorption tomography in neutron optics.

10.3.1 LinPos Tomography

Basic notions and the geometry of typical tomographic experiments are as follows. Let us assume that the sample is illuminated by parallel monochromatic pencil beams, see Fig. 10.5. Data consist of the number of particles counted behind the sample for M different scans – each scan being characterized by its horizontal position h and rotation angle φ. Alternatively, a broad illuminating beam combined with a position-sensitive detector (CCD camera) placed behind the sample can be used. In that case h labels the pixels of the camera. For the sake of simplicity a collective index $j \equiv \{h, \varphi\}$ will be used, hereafter, to label the scans.

Mean number $\bar{n}_j$ of particles (intensity) registered in j-th scan is given by the exponential attenuation law

$$\bar{n}_j = \bar{n}_0 \exp(-\int \mu(x,y) ds_j), \tag{10.16}$$

where $\bar{n}_0$ is the intensity of the incoming beam, $\mu(x,y)$ is the absorption index of the sample in position $\{x,y\}$, and the integration is the path integration along the pencil beam. This exponential attenuation law is a good approximation if scattering can be neglected. The beam hardening artifacts would also modify relation (10.16) but this complication can be avoided experimentally by the use of monochromatic beams [29].

Using neutron beams instead of X-ray photons has several advantages. Neutrons interact with the matter in a different way than photons do. Since neutrons are subject to the strong interaction, they can "see" and distinguish among different isotopes of the same element. Neutrons can also penetrate deeper into some materials such as metal surfaces, and many other objects like objects made from plastic materials often show considerably more detail when illuminated with neutrons rather than photons.

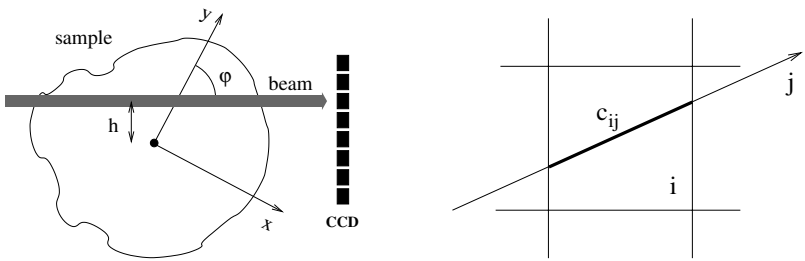

Fig. 10.5. Geometry of the experimental setup and the definition of coefficients c_{ij}.

The absorption index for thermal neutron beams can be expressed as

$$\mu(x,y) = \Sigma_{th}(x,y)\lambda/\lambda_{th}, \tag{10.17}$$

where Σ_{th} is the macroscopic thermal cross section, λ is the wavelength of the illuminating beam, and λ_{th} is the thermal wavelength. Equation (10.17) presumes a linear dependence of the involved cross sections on λ [36].

For practical purposes, it is convenient to discretize (10.16) as follows,

$$\bar{n}_j = \bar{n}_0 \exp(-\sum_{i=0}^{N} \mu_i c_{ij}). \tag{10.18}$$

The sample is now represented by a 2D mesh whose cells are assumed to be homogeneous. The variables are now N numbers μ_i specifying absorption in those elementary cells. Matrix $\{c_{ij}\}$ defines the ovelaps of beams and cells, see Fig. 10.5.

Let us first ignore the statistics of the illuminating beam, and assume that the counted numbers of particles $\{n_j\}$ do not fluctuate, $n_j = \bar{n}_j$, $\forall j$. Taking the logarithms of both sides of (10.18), one obtains a system of M linear algebraic equations for the N unknown absorption coefficients μ_i:

$$f_j = p_j, \quad j = 1 \ldots M, \tag{10.19}$$

where we defined,

$$f_j = -\ln \frac{n_j}{n_0}, \quad p_j = \sum_i \mu_i c_{ij}. \tag{10.20}$$

Notice that the problem (10.19) is a linear and positive (LinPos) problem. Its linearity is obvious, and positivity follows from the fact that no new particles are created in the sample. The importance of LinPos problems for experimental physics stems from the fact that many physical quantities, for instance mass, density, intensity, and so on, are intrinsically positive quantities that very often depend on the parameters of interest in a linear way. Linearized absorption tomography (10.19) is just one typical example taken from this wide family of problems including, among others, the measurement of focal intensity distribution for polarized input fields [37], or the characterization of the photon content of light pulses [38] to give some examples.

The inversion of (10.19) is provided by the FBP algorithm,

$$\boldsymbol{\mu} \propto \sum_{\varphi} \mathbf{f} \star \mathbf{g}, \tag{10.21}$$

where $\star$ denotes a discrete convolution of data with the regularized singular transformation kernel [39]. However, by linearity of (10.21), the positivity of the reconstructed absorption index is not guaranteed when the data is noisy.

A negative value of a reconstructed μ_i would then suggest that particles were being created in the i-th cell in the course of the experiment, which would obviously be a wrong conjecture. Another problem arises when there are only a few projections available. In such a case, the summation in (10.21) no longer approximates the original integral and unwanted artifacts appear in the reconstructions. Both these drawbacks can be avoided if the problem (10.19) is solved in the sense of maximum likelihood on the space of physically allowed absorption coefficients. In this approach one considers the data $\mathbf{f}$ and the prediction of the theory $\mathbf{p}$ as two probability distributions. One looks for absorption coefficients $\{\mu_i\}$ minimizing the Kullback-Leibler "distance"

$$D(\mathbf{f}, \mathbf{p}) = -\sum_j f_j \ln \frac{p_j}{f_j} \tag{10.22}$$

between the data $\mathbf{f}$ and theory $\mathbf{p}$. Here, a little more care is needed since $\mathbf{p}$ and $\mathbf{f}$ are generally not normalized to unity. The minimum of the Kullback-Leibler distance corresponds to the maximum of the likelihood functional [15]

$$\mathcal{L} = \prod_j \left(\frac{p_j}{\sum_k p_k} \right)^{f_j}, \tag{10.23}$$

that quantifies the likelihood of the given distribution $\{\mu_i\}$ in view of the registered data. We seek the maximum-likely distribution of the absorption indices. A convenient way to find it is the Expectation-Maximization (EM) iterative algorithm [40, 41],

$$\boldsymbol{\mu}^{n+1} = \boldsymbol{R}(\boldsymbol{\mu}^n) \cdot \boldsymbol{\mu}^n, \tag{10.24}$$

where

$$R_i = \frac{1}{\sum_{j'} c_{ij'}} \sum_j \frac{f_j c_{ij}}{p_j(\boldsymbol{\mu})}, \tag{10.25}$$

and $\boldsymbol{\mu}^0$ is some initial strictly positive distribution $\mu_i^{(0)} > 0$, $i = 1 \ldots N$. A nice feature of EM algorithm is that its convergence is guaranteed for any input data f_j [42]. For this reason it became a valuable tool in many inverse problems that can be reduced to the form of (10.19), e.g. in positron emission tomography [42–44]. The original derivation of EM algorithm is based on alternating projections on specially chosen convex sets of vectors. However, one could directly use the calculus of variations to derive the necessary condition for the extreme of the functional (10.23). Iterating these, one eventually arrives at the EM algorithm again. An advantage of this alternative derivation is that it can be also applied to more realistic physical models of the actual absorption experiment. One such possible generalization will be shown in the following subsection.

10.3.2 Tomography with Poissonian Signals

Real signals are not composed of a sharp number of particles. For instance, two kinds of signals often used in experiments —beams of thermal neutrons and laser light— both exhibit Poissonian fluctuations of the number of particles. Monochromatic neutron beams also are correctly described by the Poissonian statistics if the detected count events occur in a mutually independent manner [45]. The knowledge of the true character of the signal illuminating the sample is a useful piece of prior information, which can be utilized for improving the performance of the tomographic imaging.

As the Poissonian character of the signal is preserved during the attenuation, the counted numbers of particles behind the sample are random Poissonian variables. The corresponding likelihood functional reads,

$$\mathcal{L} = \prod_j \frac{\bar{n}_j^{n_j}}{n_j!} e^{-\bar{n}_j}. \tag{10.26}$$

This is the joint probability of counting $\{n_j\}$ particles. Their mean values $\{\bar{n}_j\}$ obey the exponential law (10.16) as before. They depend on the absorption in the sample $\{\mu_j\}$ that is to be inferred from the data. The necessary condition for the maximum of the likelihood (10.26) can be derived using the calculus of variations. The extremal equation can be shown to have the same vector form as the extremal equation of the LinPos problem (10.24) with the vector $\mathbf{R}$ replaced by

$$R_i^{(\mathrm{Poisson})} = \frac{\bar{n}_0}{\sum\limits_{j'} c_{ij'} n_{j'}} \sum_j c_{ij} \exp(-\sum_{i'} \mu_{i'} c_{i'j}). \tag{10.27}$$

When the input intensity $\bar{n}_0$ is not known, it should be estimated too:

$$\bar{n}_0 = \sum_j n_j \Big/ \sum_j \exp(-\sum_i \mu_i c_{ij}). \tag{10.28}$$

As seen, the Poissonian tomography is intrinsically a nonlinear problem. This has serious consequences for the convergence properties of the iterative algorithm (10.24) and (10.27). Instead of converging to a stationary point it might end up in oscillations. Typically, such convergence problems arise in the presence of very noisy data. When this happens, it is necessary to decrease the size of the iteration step as follows: $R_i \to R_i^\alpha, \quad i = 1 \ldots M, \quad 0 < \alpha < 1$. Of course, any solution to the regularized problem is also a solution to the original problem.

10.3.3 Comparison with Standard Methods

In real experiments there are many factors that could influence the quality of the measured data and therefore also the result of the tomography. Misalignments present in the experimental setup, instability of the illuminating

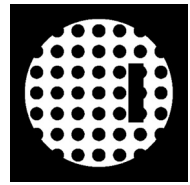

Fig. 10.6. The object.

Table 10.2. Quality of the input data. The last column shows the mean number of counted particles per pixel in the incident beam.

reconstruction	angles	pixels	intensity
a	13	161	∞
b	19	101	∞
c	20	101	∞
d	7	301	∞
e	15	161	2000

beam, white spots and damaged detector pixels can be such factors, to name a few. To avoid this problem let us first show a few simulations. The data were generated on a computer from the artificial object shown in Fig. 10.6. It is a circle made of a homogeneous material with many small round holes drilled through it. One additional rectangular piece of material was removed from the circle to make it less symmetric. The absorption index of the material was chosen in such a way that the maximum attenuation along a beam was close to 50% of the input intensity.

In the simulations, the object was subject to five different experiments. Their parameters are summarized in Table 10.2. First four experiments correspond to the ideal situation of a very high beam intensity where the Poissonian detection noise can safely be ignored. The last reconstruction simulates more realistic conditions with 2000 counts per pixel in the open beam. Notice that a relatively small number of rotations is chosen for all five experiments. In this regime the inverse Radon transformation is expected to yield bad results and the improvement of the maximum-likelihood tomography upon the standard technique should be most prominent. This regime is also important from the practical point of view. Doing more rotations implies a longer measurement time and more radiation absorbed by a sample. The latter may be an important factor if the imaging of biological samples is considered. Provided the improvement of the reconstruction technique gives comparable resolution with less data, imaging costs and damage done to a sample due to radiation might be reduced.

Reconstructions from the simulated data are shown in Fig. 10.7 [46]. The simulated data were first processed using the IDL imaging software (Research

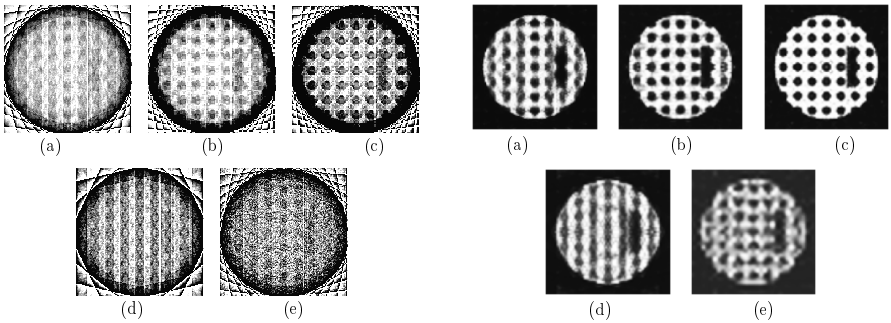

Fig. 10.7. Left panel: IDL reconstructions from the simulated data, for parameters see Table 10.2. Right panel: ML reconstructions from the same data; the iterative algorithm (10.24) and (10.27) has been used for reconstruction.

Systems Inc.) which implements the standard FBP algorithm (inverse Radon transform), see the left panel in Fig. 10.7. This software is one of the industrial standards in the computer assisted tomography. The same data were then processed using the iterative algorithm based on the maximization of the Poissonian likelihood function, see the right panel Fig. 10.7. In the absence of noise, see cases (a)-(d), the fidelity of a reconstruction depends on two main factors—the spatial resolution of the detector, and the number of rotations used. It is apparent from Fig. 10.7 that the latter factor is the more important of the two. Very small number of angles cannot be compensated by an increased spatial resolution of the detector, compare e.g. cases (c) and (d), and reconstruction (d) is by far the worst one. However, ML tomography is much less sensitive to the number of angles than the standard filtered back-projection. Even the large rectangular hole in the object is hardly perceptible in the IDL reconstruction (d) in Fig. 10.7, whereas it nicely shows in the ML reconstruction from the same data. ML reconstructions are superior to the standard ones also in cases (a)-(c); notice that the ML reconstruction (c) that is based on as few as 20 different angles is nearly perfect.

Benefits of the ML tomography are fully revealed when the detected data are noisy. This is case (e) in Table 10.2. Standard filtered back-projection applied to noisy data faces serious difficulties. This is due to ill-posedness of the Radon transformation where data are integrated with a singular filter function. Obviously such deconvolution greatly amplifies any noise present in the data. Having little or no prior information about the object it is difficult to tell true details of the object from artifacts. ML tomography gives much better results. Since noises are incorporated into the algorithm in a natural and statistically correct way, artificial smoothing is not needed. Notice in simulation Fig. 10.7e that the noisy data yields through the ML algorithm a little distorted but otherwise clear image, unlike the corresponding very noisy standard reconstruction. This is a nice feature of the intrinsically non-

linear ML algorithm, which, in the course of reconstruction, self-adapts to the registered data and always selects the most likely configuration.

10.3.4 Strongly Absorbing Materials: An Experiment

One specific application of neutron CT imaging is the quantitative analysis and three-dimensional visualization of the ^{10}B isotope distribution in boron alloyed steel. Boron alloyed steel is used in nuclear engineering as neutron shielding for the radioactive waste disposal equipment, such as components for the compact fuel storage racks and transportation baskets. The main demand on the sheets for these applications is, besides mechanical stability and corrosion resistance, the largest possible thermal neutron attenuation, which has to be uniform over the whole volume. The attenuation in the steel depends mainly on the ^{10}B isotope, which has a large attenuation cross section for thermal neutrons $\sigma_{th}(^{10}B) = 3838.1(10) \times 10^{-24}\text{cm}^2$ [47].

Imaging of strongly absorbing samples suffers from the beam hardening effect. The wavelength dependence of scattering cross section (10.17) causes a spectral change of the neutron flux in the sample, where preferably low energy neutrons are absorbed so that the remaining beam becomes richer in high energy neutrons. Besides this effect, the following specific difficulties occur with strong absorbing materials:

- The exposure time for one projection is several minutes and the total measurement time for one tomographic data set lasts several hours. If the data are analyzed with the FBP algorithm, one depends on a stable operation of the neutron source and CCD detector.
- The low count numbers lead to increased statistical fluctuations which get amplified in the FBP reconstruction.
- The imaging quality depends strongly on low background conditions. The contribution of scattered thermal neutrons, fast neutrons, gammas, and light penetration in the detector box has to be suppressed as far as possible.
- The stronger the attenuation in the sample, the more the result will interfere with the choice of input parameters in the FBP routine.

All these reasons clearly favor ML statistical inversion over the deterministic FBP algorithm.

Let us show some examples of the tomographic investigations of strong absorbers that were performed at the 250 kW TRIGA reactor of the Atominstitut in Vienna, where at a well-thermalized beamline, a neutron-tomography facility had been implemented [48]. Surprisingly, neutron-tomography of strong absorbers is still possible with weak beam intensities of about $10^5\text{n/cm}^2\text{s}$. High resolution camera optics with the nominal resolution of 80μm was used [48]. During the experiment, only a few neutrons per second per pixel were registered. Naturally, the discrete character of the quantum signal plays an important role at such low intensities.

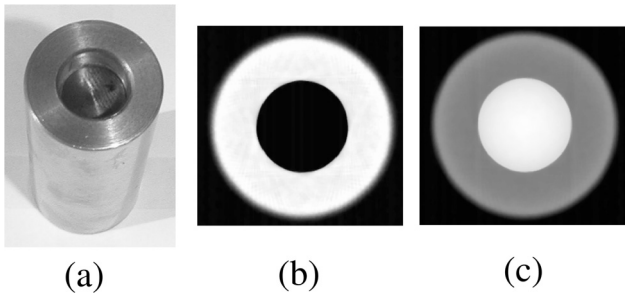

Fig. 10.8. Measured steel sample. This is a two component system, which consists of an outer ring ($\emptyset$ = 2 cm), partly filled with a second rod with 68% enlarged boron content ($\emptyset$ = 1 cm). Expected distribution of the absorption index in the upper hollow (b) and lower filled (c) regions are also shown [30].

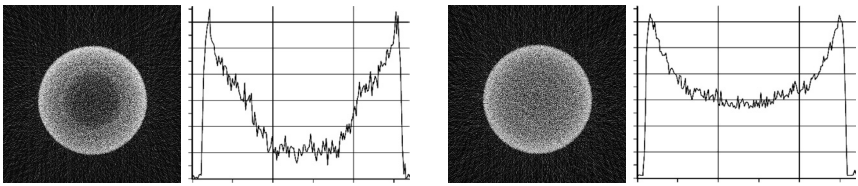

Fig. 10.9. FBP reconstructions of the sample shown in Fig. 10.8. 50 different projections were used. (a) A typical reconstructed cut through upper region, where instead of the second rod only an air hole is inside the ring; (b) a typical reconstructed cut through the middle region, where the second steel rod with higher boron content is inside the ring. The noise in the profile plots was suppressed by averaging over several tens of reconstructed slices.

The measured sample, see Fig. 10.8 was a two-component system consisting of a ring with an outer diameter of 2 cm and a hole of 1 cm diameter. The hole was partially filled with a second rod of 1 cm diameter with somewhat larger ^{10}B content.

First we will show some typical results obtained with the standard FBP algorithm, see Fig. 10.9. Notice, that despite a large number of projections (angles) that were used for the inversion, the reconstructions are still rather noisy. Also, the reconstructed absorption profiles are far from the expected ones. This is caused partly by the previously mentioned beam hardening effect that was not taken into account here.

Figure 10.10 illustrates the usefulness of the ML technique in cases where only a few projections are available. The reconstructions are based on the same experimental data as the corresponding Figs. 10.9a and 10.9b. However, the number of projections was reduced from 50 to just 10 (!) projections. In this extreme case the filtered back-projection fails completely. It is interesting to notice that although no correction of the beam hardening effect was done

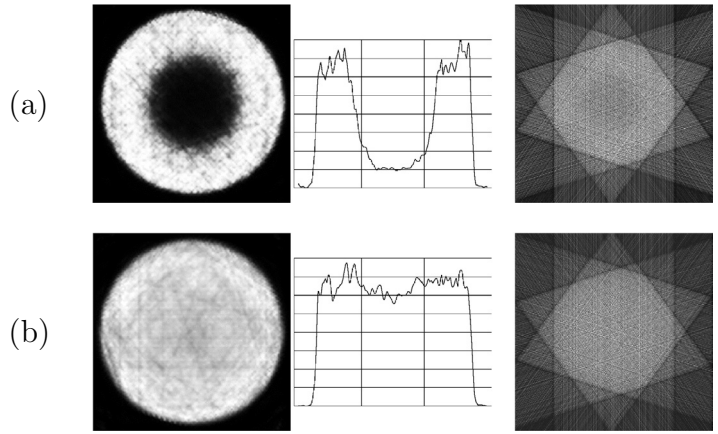

Fig. 10.10. Reconstructions of the sample of Fig. 10.8 from only 10 (!) projections; panels (a) and (b) correspond to slices shown in Figs. 10.8b and 10.8c, respectively. Left: ML reconstructions; middle: ML profiles; right: standard FBP interpretation of the same data is shown for comparison.

during the ML reconstruction, the reconstructed density profiles resemble the true density profiles more closely than the corresponding FBP profiles shown in Fig 10.9. Also the quality of the ML reconstruction from 10 projections is not inferior to FBP results obtained from data sets that are five times larger. A proper statistical treatment extracts more information from the measured data than the standard reconstruction methods do. In this way, the measurement time can be significantly reduced without loss of resolution. Still better results can be expected provided the beam hardening is incorporated into the physical model.

10.4 ML Neutron Phase Tomography

10.4.1 Experimental Setup

The absorption tomography discussed in the previous section provides only partial information about the object of interest. Optical properties of objects are more completely described by the distribution of the complex index of refraction $n(x, y)$, whose real part called simply index of refraction, and imaginary part called index of absorption are responsible for the phase shift and absorption of the illuminating beam, respectively. It is clear that for the 3D visualization of the index of refraction some kind of interferometric technique is needed. In a sense, phase tomography is a combination of both the previously mentioned inverse problems — the phase estimation discussed in Sect. 10.2 and tomographic imaging discussed in Sect. 10.3.

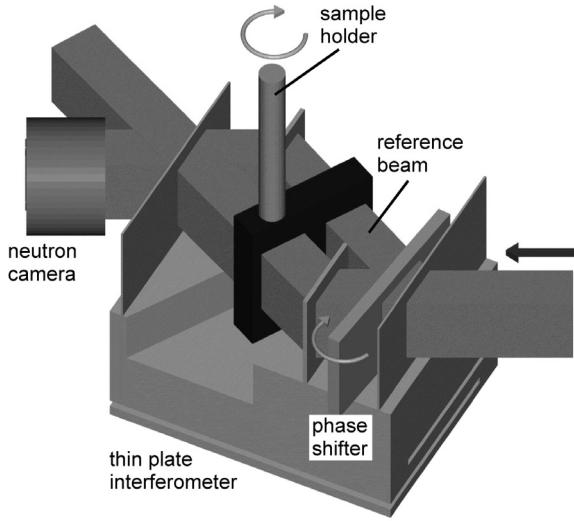

Fig. 10.11. Scheme of an nPCT experiment.

As has been already mentioned, in neutron optics one is often confronted with low count numbers because the phase space density of present neutron beams is 30 orders of magnitude below that of laser beams and many orders below X-ray sources. This intensity problem has dramatically arisen in the recently developed neutron phase contrast tomography (nPCT) [49]. PCT was originally invented in X-ray tomography with much higher coherent intensities available [50–52]. In order to utilize nPCT it is necessary to develop an advanced reconstruction technique, which can be applied to very low count numbers. For instance, the typical count number in present nPCT setups is around 200 n/2h in a $50 \times 50\rangle\mu m^2$ pixel. In principle, focusing techniques, e.g. asymmetric Bragg reflections, can enhance the density of quasi-monochromatic neutron beams, but such hypothetic gains will be used to reduce the measurement time rather than to raise the count numbers. Therefore the low numbers of detected neutrons have to be accepted as the limiting factor of nPCT.

A strong motivation for developing nPCT is its extreme sensitivity, which is at least three orders of magnitude higher than in the conventional absorption tomography. The nPCT method proves its strength in extreme applications where other methods fail: (i) 3D investigation of non or weak-absorbing substances, (ii) analysis of isotope distributions with high sensitivity, (iii) investigation of magnetic domains in bulk materials [53], and (iv) energy and momentum exchange free analysis of magnetic (axial) and scalar potentials.

The experimental setup of nPCT is schematically shown in Fig. 10.11. The sample is inserted into one arm of a perfect crystal interferometer while an object of known characteristics placed in the other arm compensates the

large overall phase shift introduced by the thick sample. The output beam is then registered by a CCD camera with the spatial resolution of $50\mu m$. Like in the absorption tomography, the sample is rotated around the vertical axes and up to several tens of scans are registered. Angle φ together with the position h of a CCD pixel specify the path of the particles registered by that pixel through the sample, see Fig. 10.5. For the sake of brevity, they will again be represented by a single collective index j.

To get an unambiguous value of the reconstructed phase, a set of auxiliary phases δ_j, controlled by the experimenter, is needed for the estimation. They are provided by an auxiliary phase shifter, see Fig. 10.11, and the resulting interferograms are simply called scans or phase projections [54]. In nPCT their number should be chosen as less as possible so as to minimize the measurement time.

The conceptual difference between the standard deterministic and ML statistical inversions can be nicely illustrated on the example of nPCT. Standard nPCT consist of two separate steps: First, each set of interferograms is processed to get the distribution of the total phase accumulated in the j-th scan; this total phase is an integral of the unknown index of refraction along the j-th beam path. In this way, the original problem is reduced to the conventional tomographic imaging, and hence the inverse Radon transformation of the accumulated phase yields the distribution of the index of refraction within the object.

This straightforward procedure suffers from all known shortcomings of the standard FBP routine, which are further accented in nPCT by still smaller measured intensities and thus increased fluctuations. Additional problems arising in the standard nPCT are caused by using the accumulated phases as the starting point for tomographic reconstruction. Due to the high phase sensitivity it is very likely that some of the projected (accumulated) phases will exceed 2π phase interval. The correction of these "phase jumps" becomes virtually impossible if the data are very noisy.

Most of these problems can be avoided when the ML statistical inversion is adopted. Here, the object is decomposed into many elementary cells each shifting the phase of the overlapping beam by only a fraction of the 2π phase window. Thus the phase value of each cell is uniquely defined. Then we look for such distribution of those elementary phases that is most likely from the point of view of registered data. In this way, phase estimation and tomographic reconstruction are done simultaneously.

10.4.2 ML Reconstruction Algorithm

Let us first discuss phase estimation in the context of nPCT. Consider an interferometric measurement with mean intensity N and amplitude V. The interference pattern,

$$\bar{n}_\alpha = N + V\cos(\theta + \delta_\alpha), \tag{10.29}$$

will be scanned with L different settings of the auxiliary phase shifter uniformly distributed over the 2π phase window,

$$\delta_\alpha = \alpha \frac{2\pi}{L}, \quad \alpha = 0, 1, \ldots, L-1. \tag{10.30}$$

Interference pattern (10.4) is just a special case of (10.30) corresponding to $L = 4$ phase shifts.

When the measurement is over, all the accumulated information can be expressed as an *a-posteriori* likelihood function. It is essential that the likelihood includes all measured data, and, together with the physical model for the detection probabilities, all experimental evidence. Thus, the likelihood is the optimum starting point for a complete tomographic analysis.

Ideally, the only fluctuating quantity in the tomographic measurement is the counted number of particles. The fluctuations produced by thermal sources such as nuclear reactors are well described by the Poissonian statistics, which was confirmed in several experiments [45,55]. Since the detections with different settings δ_α are independent, the joint probability of registering data $\mathbf{n}$ is simply a product

$$\mathcal{L} = \prod_\alpha \left(\bar{n}_\alpha^{n_\alpha} e^{-\bar{n}_\alpha} / n_\alpha! \right). \tag{10.31}$$

This is also the likelihood of the given value θ of the unknown phase shift.

In accordance with the maximum-likelihood principle we will take the maximum likely phase as the inferred value of θ. Since the amplitude V and the total mean number of particles N are not under experimenter's control and may vary from one pixel to another, these parameters should be estimated together with phase. Their values are found by maximizing function (10.31), or its logarithm. The latter in the case of uniformly distributed auxiliary phase shifts simplifies to

$$\log \mathcal{L} \propto \sum_\alpha n_\alpha \log[N + V \cos(\theta + \delta_\alpha)] - NL + \text{const.}. \tag{10.32}$$

Now it is convenient to introduce new variables $x = V \cos\theta$ and $y = V \sin\theta$. We are looking for the point where the likelihood has zero slope: $\partial\mathcal{L}/\partial x = \partial\mathcal{L}/\partial y = \partial\mathcal{L}/\partial N = 0$. From (10.32) we get the following extremal equations:

$$\sum_\alpha \frac{n_\alpha \mathbf{X}}{N + x\cos\delta_\alpha - y \sin\delta_\alpha} = 0, \quad \mathbf{X} = (\cos\delta_\alpha, \sin\delta_\alpha, \mathbf{1}). \tag{10.33}$$

In general, these equations must be solved numerically. Closed-form solution can be found only in some special cases such as $\alpha = 3$ and $\alpha = 4$.

A particularly simple solution exists for three auxiliary phases, when the maximum of the Poissonian likelihood (10.31) coincides with the maximum

of its Gaussian approximation,

$$\mathcal{L} \propto \exp\Big[-\frac{1}{2\sigma^2}\sum_{\alpha}(n_\alpha - \bar{n}_\alpha)^2\Big], \tag{10.34}$$

yielding

$$x = \frac{2}{L}\sum_{\alpha=0}^{2} n_\alpha \cos(-\delta_\alpha), \quad y = \frac{2}{L}\sum_{\alpha=0}^{2} n_\alpha \sin(-\delta_\alpha), \quad N = \frac{1}{L}\sum_{\alpha=0}^{2} n_\alpha. \tag{10.35}$$

These, going back to the original variables, can be written in the following compact form [19]

$$V = 2|R|/L, \quad e^{i\theta} = R/|R|, \tag{10.36}$$

where

$$R = \sum_{\alpha=0}^{2} n_\alpha e^{-i\delta_\alpha}. \tag{10.37}$$

This quantity can be interpreted as the first coefficient of the discrete Fourier transformation of the registered counts n_α [23].

Therefore it is particularly useful to use three auxiliary phase shifts, for in that case, the optimal phase estimation is easily handled by means of the simple formula (10.36).

In nPCT, phase sensitive data $n_{j\alpha}$ are registered. Subscripts j and α label scans (i.e. pixels of the CCD camera and rotations of the sample) and auxiliary phases, respectively. As each scan contributes likelihood (10.34) and different scans are independent observations, the total log-likelihood reads

$$\log \mathcal{L} \propto \sum_{j}\sum_{\alpha}(n_{j\alpha} - \bar{n}_{j\alpha})^2 + \text{const.}, \tag{10.38}$$

where the mean number of particles detected in the j-th projection is given by

$$\bar{n}_{j\alpha} = N_j + V_j \cos(\theta_j + \delta_\alpha + \theta_j^r). \tag{10.39}$$

Here θ_j is the total phase accumulated along the j-th projection, $\theta_j = \sum_i c_{ji}\mu_i$. Coefficients c_{ji} are the overlaps between the j-th projection and the i-th elementary cell of the reconstruction mesh, as before, see Fig. 10.5, and θ_j^r are the reference phases describing the phase properties of the empty interferometer. The latter can be estimated from the same set of projections measured without the sample. Likelihood (10.38) is to be maximized over the distribution μ_i of the optical density of the sample.

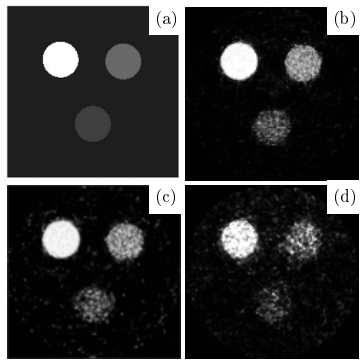

Fig. 10.12. Simulated phase tomography with a weak neutron signal. The maximal accumulated θ_j in the three cylinders making up the object (a) are 150 deg., 50 deg, and 30 deg for white, light gray, and dark gray, respectively. The mean count numbers per pixel and visibilities are (b) $N = 450$, $V = 33\%$; (c) $N = 150$, $V = 33\%$; (d) $N = 30$, $V = 33\%$.

In neutron phase imaging, μ is composed of the sum of all scattering length densities (Nb) of the isotopes contained in the sample:

$$\mu = -\lambda \sum_l N_l \, b_l = -\lambda \sum_l \frac{N_A \rho_l \, b_l}{A_l} \tag{10.40}$$

N_l represents the number of isotopes l per unit volume, ρ_l the isotope density, N_A the Avogadro constant ($6.02214199(47) \times 10^{23}$ mol^{-1}) and A_l the atomic weight. Parameter λ is the mean wavelength of the quasi-monochromatic beam, and b_l the coherent scattering length, which is a constant interaction parameter. Most isotopes have a positive coherent scattering length but some are known with negative b_l. The coherent scattering length is defined positive for repulsive optical potentials $\bar{V} > 0$ with the index of refraction less than unity: $n = \sqrt{1 - \bar{V}/E} = 1 - \lambda^2 N b_l / 2\pi$. The existence of positive and negative phase shifts is a speciality of neutron optics and can be utilized for fading out unwanted phase contributions.

A necessary condition for the maximum of $\log \mathcal{L}$,

$$\frac{\partial \log \mathcal{L}}{\partial \mu_i} = 0, \quad \forall \mu_i, \tag{10.41}$$

yields on using (10.38) and (10.39) the following set of extremal equations,

$$\mu_i = \mu_i \frac{\sum_j V_j c_{ji} \sin\theta_j \mathrm{Im}\{R_j\}}{\sum_j V_j c_{ji} \cos\theta_j \mathrm{Re}\{R_j\}}. \tag{10.42}$$

These can be solved numerically by repeated iterations.

Figure 10.12 shows a simulation of a nPCT experiment with various intensities and visibilities of the illuminating beam. The artificial object was scanned from 31 different angles with a resolution of 81 pixels.

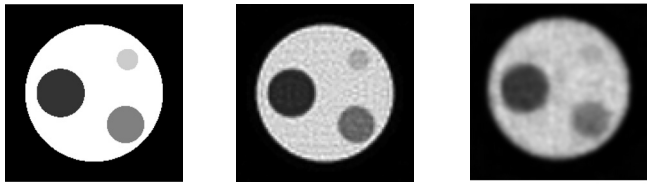

(a) (b) (c)

Fig. 10.13. Simulated phase tomography with a weak neutron signal, $N = 150$ and $V = 33\%$. The maximal accumulated θ_j in the object is 4.2π rad. (a) the artificial object; the ratio of the index of refraction in the white, light gray, dark gray, and black cylinder is $1 : 0.8 : 0.5 : 0.2$. (b) ML reconstruction from 31 angles and 81 pixels. (c) ML reconstruction from 21 angles and 41 pixels.

Case (d) is the most interesting one. Here the incident beam has such a low intensity that its Poissonian fluctuations are comparable to the intensity changes caused by the maximal phase shifts in the light gray and dark gray cylinders. The useful phase information is thus almost lost in the background noise, yet all three cylinders nicely show in the reconstruction.

Another example of the ML phase tomography is shown in Fig. 10.13. The parameters of the simulated experimental setup are comparable to that of Fig. 10.12 but now the maximal phase shift in the sample is well in excess of 4π radians. A priori knowledge about the shape and high index of refraction of the white container could be easily incorporated into the reconstruction, and as a result the internal structure of the object was nicely resolved.

A similar isotope gauge, a mixture of S33+S34 and H2O+D2O isotopes, has recently been investigated at the nPCT setup ILL-S18 in Grenoble in order to verify the sensitivity and spatial resolution of present nPCT.

10.4.3 Reference Phase Measurement

No interferometers are perfect. Already an empty interferometer shows a nonuniform transversal distribution of phase difference between its two arms. To get rid of this background phase the measurement is done in two steps: with and without the sample. The most simple way how to subtract the background phase is to perform two separate phase reconstructions, then subtract the reconstructed background phase from the reconstructed phase of the sample. This procedure is simple, but not optimal. It is not difficult to see why. The inspection of (10.42) shows that the reconstructed indexes of refraction μ_i depend on the visibilities V_j of the registered interference fringes. This is natural since the reconstruction is a synthesis of many phase measurements and phases measured under higher visibility are less affected by the noise and hence more credible. For the same reason the phase introduced by an empty interferometer is measured more accurately that phase introduced by interferometer **and** sample. This additional knowledge should be incorpo-

rated into the reconstruction routine. Denoting $\theta = \theta_s + \theta_r$ the total phase measured with the sample, which is the sum of the reference phase and phase introduced by the sample θ_s, and using (10.36) and (10.37) in (10.34) we can rewrite the posterior distributions of θ and θ_r in the following compact form:

$$P(\theta) \propto e^{V\cos(\theta-\theta_{\mathrm{NFM}})} \tag{10.43}$$

$$P(\theta_r) \propto e^{V_r\cos(\theta_r-\theta_{r,\mathrm{NFM}})}. \tag{10.44}$$

NFM denotes Gaussian (semi-classical) phase estimates that maximize posterior distributions (10.43) and (10.44), which are also known as von Mieses normal distributions defined on the unit circle. As has been mentioned above their widths are determined by visibilities. As we are interested only in phase θ_s introduced by the sample alone, let us calculate its posterior distribution,

$$P(\theta_s) = \iint P(\theta)P(\theta_r)\delta(\theta-\theta_r-\theta_s)d\theta_r d\theta. \tag{10.45}$$

The double integrations can be easily carried out, and the result expressed in terms of the Bessel function I,

$$P(\theta_s) \propto I_0\left(\sqrt{V^2+V_r^2+VV_r\cos(\theta_s-\theta_{-,\mathrm{NFM}})}\right), \tag{10.46}$$

where $\theta_{-,\mathrm{NFM}} = \theta_{\mathrm{NFM}} - \theta_{r,\mathrm{NFM}}$. Optical density of the sample can now be estimated by maximizing the posterior distribution (10.46) with respect to indexes μ_i. Such procedure accounts for the reference phases in an optimal way.

10.4.4 Beyond Phase Tomography

Phase tomography discussed in the previous section is a simple example of the quantum-process tomography. In this case the process is a unitary operation that can be represented by a 2D rotation. The rotations vary in space, and the detected particles probe their spatial distribution via quantum interference.

Obviously, to "see" more complicated transformations, more complex probes are needed. It would be logical to proceed the exposition with the case of spin 1/2 systems whose Hilbert space could be associated with the 3D Bloch sphere. The synthesis of measurements - projections, is capable to determine an unknown quantum state, and such procedure posses all the features of quantum tomography of the internal spin state. ML approach according to the general receipt given in chapter by Hradil *et al.* in this volume can be straightforwardly applied here. This was worked out explicitly in [56] for the representation of the spin using the polarization vector.

Since magnetic momentum of particles is coupled to the magnetic field, spin state tomography can be used as a means e.g. for non-destructive investigations of the magnetic domains of bulk materials. Here the beam of

polarized neutrons goes through the specimen interacting with its magnetic domains. Due to this interaction, the spin state of neutrons changes, and this depolarization can be utilized for the visualisation of the magnetic domains in the specimen just like in the case of phase tomography. However, the probed operations are now represented by rotations in 3D space, which unlike 2D rotations in phase tomography form a non-Abelian group of transformations. Consequently, the tensorial character of the corresponding depolarization observable together with the non-commutativity of rotation matrices makes the analysis rather involved. Though this is a challenging question with potential interesting applications, at present no analytical solution of this inverse scattering problem is known. Up to now there are several approaches based on deterministic techniques, but ML solution has not been devised yet.

10.5 Maximum-Likelihood Characterization of Photonic Qutrits

Apart from using spin 1/2 particles as probes for sensing and visualization of physical fields they can also be utilized for the physical realization of qubits in the newly emerging field of quantum information processing. Much attention has recently been turned to exploring the possibilities of applying quantum systems in communication and computing protocols. Usually, these protocols use the information encoded in such bidimensional systems. Nevertheless, some proposals show that higher dimensional systems are better suited for some purposes [57–64]. On a more fundamental level, higher dimensional spaces provide with counter-intuitive examples of the relationship between the quantum and the classical information, which cannot be found in two-dimensional systems [65].

Recently, some experimental implementations of higher dimensional quantum systems have appeared. Given the high technical status of photonic technology and the fact that photons will for a long time remain the only means for quantum communication, it is desirable to have qunits (systems with n different orthogonal states) to be carried by photons. Encoding qunits with photons has already been experimentally demonstrated using interferometric techniques, with time-bin schemes [66] and superpositions of spatial modes [67]. Up to now, the only non-interferometric technique of encoding qunits in photons is using the orbital angular momentum (OAM) of the photons or, equivalently, the transversal modes [68–74].

Before we apply ML technique to the reconstruction these higher dimensional states let us first review some basic facts about the quantum states of orbital angular momentum degrees of freedom of light.

On theoretical grounds, one convenient basis which describes the transversal modes of a light beam fulfilling the paraxial approximation is the Laguerre-Gaussian (LG) functions basis: $LG_{p,m}(x, y)$. Here m is the order of the phase dislocation characteristic of this set of functions and it accounts

directly for the orbital angular momentum of the Laguerre-Gaussian mode in units of $\hbar$ [75–77]. The other parameter p is a label which is related to the number of radial nodes of the mode and (x, y) refer to any point in a plane perpendicular to the beam propagation direction. The LG functions form a complete and orthonormal basis for any complex function in the transveral plane.

Holographic techniques, among other schemes, can be used to transform LG modes [78,79]. Conveniently prepared holograms change the phase structure of the incoming beam, adding or removing the phase dislocations related with the orbital angular momentum. Whereas optical single mode fibers act as a filter for all higher LG modes, i.e. only the LG_{00} can be transmitted, the combination of holograms and single mode fibers project the incoming photon into different states. In this way we can define the basis of the experimentally accessible states as:

$$\langle \boldsymbol{x}|0\rangle = LG_{0,0}(x, y), \quad |m\rangle = H_m(\mathbf{0})|0\rangle, \tag{10.47}$$

where the vector $|0\rangle$ represents the effect of using only a single mode fiber to detect the photon, $\boldsymbol{x}$ is a shortcut to represent any point in the transversal space[5], m is a positive or negative integer, and $H_m(\mathbf{0})$ is the operator which describes the action of the m-th order hologram when it's centered, relative to the fiber. Explicitly, the expression of this operator is

$$\langle \boldsymbol{x_1}|H_m(\mathbf{0})|\boldsymbol{x_2}\rangle = \exp(-im \arctan(\frac{y_1}{x_1}))\delta(x_1 - x_2, y_1 - y_2). \tag{10.48}$$

Albeit by construction, any of the modes in our basis posses orbital angular momentum of m, they are not pure LG-modes. However, they can be described as coherent superpositions of different modes with the same m, but different p's. In this sense, the base we have constructed in (10.47) is orthonormal[6], although not complete, since it does not expand the complete LG basis. In the following we refer to all modes belonging to the subspace (10.47) as "inner" modes and the rest of the modes will be addressed as "outer" modes.

Thus, any displaced hologram and, in general, any linear operator which acts on our Hilbert space can be expressed like,

$$H_m(a, b) = \sum_{i=-\infty}^{+\infty} c_i(a, b)H_i(0) + \gamma(a, b)\Gamma, \tag{10.49}$$

where a, b are the displacements of the hologram relative to its centered position. The operator Γ accounts for the possibility that the displaced hologram

[5] The transversal position of a photon can only be accounted under the paraxial approximation.

[6] The normality of the functions comes from the fact that $\langle 0|0\rangle = 1$ and that the hologram operations are unitary.

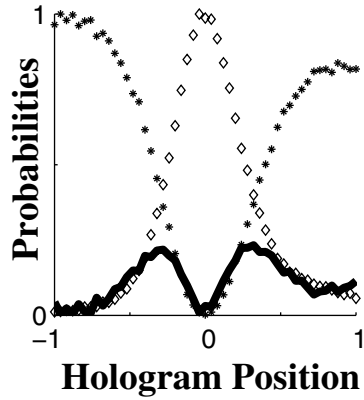

Fig. 10.14. Experimentally measured transfer of the $|0>$ mode to "outer" modes depending on the position of the hologram. The solid line represents the measured normalized value of $1-\sum_{i=-1}^{+1}|<i|H_m(x,0)|0>|^2$, where x is the position of the hologram in the x-axis. Other $|m>$ modes only contribute slightly to this value. The dashed lines represent the normalized measured values of $|<0|H_m(x,0)|0>|^2$ and $|<1|H_m(x,0)|0>|^2$, and are presented for the sake of comparison. The maximum transfer to "outer" modes happens around the position where $|<0|H_m(x,0)|0>|^2=|<1|H_m(x,0)|0>|^2$.

is performing transformations between "outer" and "inner" states, i.e. transforming any "inner" state into an "outer" one, or the other way round.

The value of γ can be estimated by

$$|\gamma(a,b)|^2 \sim 1-\sum_{i=-\infty}^{+\infty}|\langle i|H_m(a,b)|0\rangle|^2, \tag{10.50}$$

which is a feasible observable. In Fig. 10.14 we present an example of such a measurement. The data was taken by preparing a photon in the $|0\rangle$ state, and transforming its state by means of a hologram of order $m=+1$, which could be displaced along the horizontal x-axis. Afterwards, the transformed photon was projected onto three dimensional OAM Hilbert space consisting of $|-1\rangle$, $|0\rangle$ and $|1\rangle$. The other $|m\rangle$ states have a much smaller contribution than the one due to "outer" states. In Fig.10.14 there are two positions where the contribution of the "outer" modes is specially high. These positions roughly correspond with an equal superposition of the two higher modes, i.e. $|c_0|=|c_1|$.

10.5.1 Experimental Set-Up

The experimental set-up is shown in Fig. 10.15. A 351nm wavelength Argon-ion laser pumps a 1.5−mm-thick BBO (β-barium-borate) crystal cut for

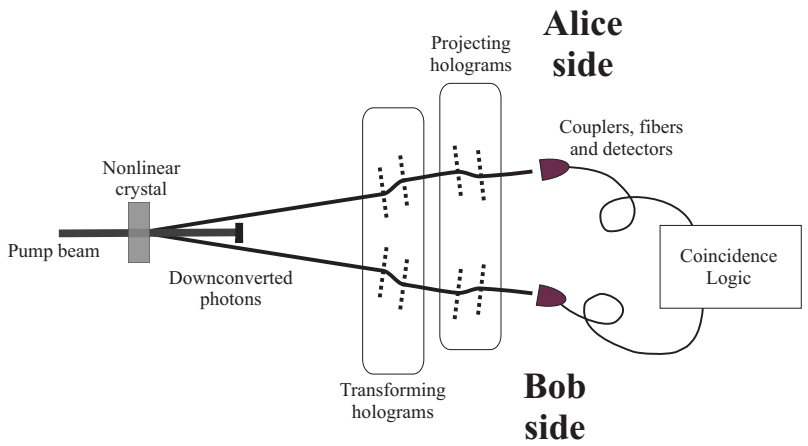

Fig. 10.15. Experimental set-up. A 351nm wavelength laser pumps a BBO crystal. The two generated 702nm down-converted photons are send to Alice and Bob's sides respectively. Before being detected each photon propagates through four different holograms.

Type I phase matching condition. The crystal is positioned to produce down-converted photons at a wavelength of 702nm emitted at an angle of 4° off the pump direction. These photons are directly entangled in the orbital angular momentum degree of freedom. In the actual protocol, an observer which we call Alice, possess the source and can manage one of the downconverted photons, meanwhile the other downconverted photon is sent to another observer, which, following a long tradition, we call Bob. Before being detected, each of the two down-converted photons traverses four holograms which we divide in two sets. Each set consists of one hologram with charge $m = 1$ and another with charge $m = -1$. The first set of holograms provides the means of a rotation in the three dimensional space expanded by the states $|-1\rangle$, $|0\rangle$, and $|1\rangle$. The second set, together with a single mode fibers and a detector, act as projectors onto the three different basis states.

In the experiment, the tomographic reconstruction of Bob's received qutrit state was realized in two independent steps trying to avoid any bias from 'a priori' information. First, the team from University of Vienna projected the photons in Bob side. The minimum number of measurements to reconstruct the three dimensional state is 9. This number increases to 121 because of our enlargement to a 11-dimensional Hilbert space. In the end, to explode the power of the ML reconstruction and to minimize errors, the number of different projections was set around 2400.

As will be shown below in all the cases, the reconstructed three dimensional state was a coherent superposition of the three "inner" vectors, which relative weights and phases could be effectively controlled. The noise and incoherence corresponded to a probability of less than 2%.

10.5.2 Experimental Measurements

Prior to the measurement taking procedure, the rotating set of holograms was analyzed to properly describe the transformation done. From the description of each single hologram, we could express the action of each transformation set in the following way:

$$\begin{aligned}\langle \boldsymbol{x_1}|H_1(a_{+1},b_{+1})H_{-1}(a_{-1},b_{-1})|\boldsymbol{x_2}\rangle = \exp(-i\arctan(\frac{y_1-a_1}{x_1-b_1}) \\ + i\arctan(\frac{y_1-a_{-1}}{x_1-b_{-1}}) - ik_x x_1 - ik_y y_1)\delta(x_1-x_2, y_1-y_2),\end{aligned} \tag{10.51}$$

where k_x and k_y are free parameters which depend on the alignment procedure, and $a_{\pm}1, b_{\pm}1$ represent the displacements of the two holograms. Each set of holograms is then described completely by eight parameters: the number of maximum coincidences, the width of the beam, four numbers to determine the centered position of each hologram and the two parameters k_x and k_y.

The estimation of these eight parameters was performed by fitting four different experimental curves as shown in Fig. 10.16. The data which conformed the curves were taken by sending to Bob a photon prepared in the $|0\rangle$ state. Bob fixed one of his holograms in one determined position and performed a scan on one of the axis of the other hologram. The resulting state was again projected to the $|0\rangle$ state, i.e. one of this curves can be described with the following number $\langle 0|H_1(x,0)H_{-1}(1,1)|0\rangle$ as a function of x. Each

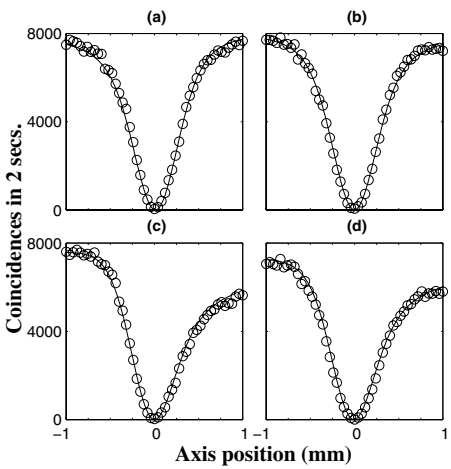

Fig. 10.16. Curve fitting for a set of holograms. First row and second row correspond to a hologram of charge $m = +1$ and $m = -1$ respectively. Left and right columns correspond to scans of the x and y axis respectively. Circles are experimental measurements. Solid line correspond to the estimated result using (10.51) and $|0\rangle$ as initial and final states.

of the four curves corresponds to the scan of the four different axis of the holograms.

The projections measurements were made by moving the set of two holograms into around 2400 different positions and counting the number of coincident detections which took place in two seconds. The complete time for each of this measurements was around six hours, due mainly to the software to access the different motors. After this time some slight misalignments where detected, which could be compensated mainly due to the large number of different projections taken and the reconstruction process

10.5.3 Results

The registered data were processed using the maximum-likelihood reconstruction algorithm. Notice that the measurement is incomplete, $\sum_j |j\rangle\langle j| \neq 1$, where $|j\rangle = H_1(a^j_{+1}, b^j_{+1})H_{-1}(a^j_{-1}, b^j_{-1})|0\rangle$ are the projections done. This has been taken into account, see Hradil *et al.* in this volume for more details.

From the technical point of view, the ML reconstruction was done by iterating the extremal equation [80],

$$R\rho R = G\rho G, \quad R = \sum_j \frac{n_j}{p_j}|j\rangle\langle j|, \quad G = \frac{\sum_j n_j}{\sum_j p_j}\sum_j |j\rangle\langle j|, \tag{10.52}$$

starting from the maximally mixed state Here n_j is the number of photon pairs found in state $|j\rangle$ and $p_j = \mathrm{Tr}\{|j\rangle\langle j|\rho_{\mathrm{Bob}}\}$ are the corresponding probabilities.

Let us mention that though the reconstruction is done on the full $3 + 8$ dimensional Hilbert space spanned by the "inner" and "outer" states, we are interested only in the former subspace. Therefore all the reconstructed states are projected to this subspace to simplify the discussion.

As we have already mentioned, different projections done by Alice translate through the entanglement to different state preparations on Bob's side. Four such remote preparations are shown in Fig. 10.17. All of them were found to be very nearly pure states, their largest eigenvalues and corresponding eigenvectors being (a) $\lambda_{max} = 0.99$, $|e_{max}\rangle = (0.31+0.61i)|0\rangle+0.71|-1\rangle$; (b) $\lambda_{max} = 0.97$, $|e_{max}\rangle = (0.2+0.16i)|0\rangle+0.68|1\rangle+(0.68-0.05i)|-1\rangle$; (c) $\lambda_{max} = 0.99$, $|e_{max}\rangle = 0.65|0\rangle+(-0.18-0.52i)|1\rangle+(-0.18-0.5i)|-1\rangle$; (d) $\lambda_{max} = 0.99$, $|e_{max}\rangle = (-0.54+0.2i)|0\rangle+0.58|1\rangle+0.58i|-1\rangle$. In case (a) Alice tried to prepare an equal-weight superposition of $|0\rangle$ and $|-1\rangle$ basis states. Utilizing the conservation of the orbital momentum in downconversion, this was easily done by projecting her qutrit along the ray $|0\rangle+|1\rangle$: Her hologram with the positive charge was taken out of the beam path and the center of the other other one was displaced with respect to the beam by a calculated translation vector. In case (b) the remotely prepared state supposed to be an equal-weight superposition of $|-1\rangle$ and $|1\rangle$ states. Here both holograms had

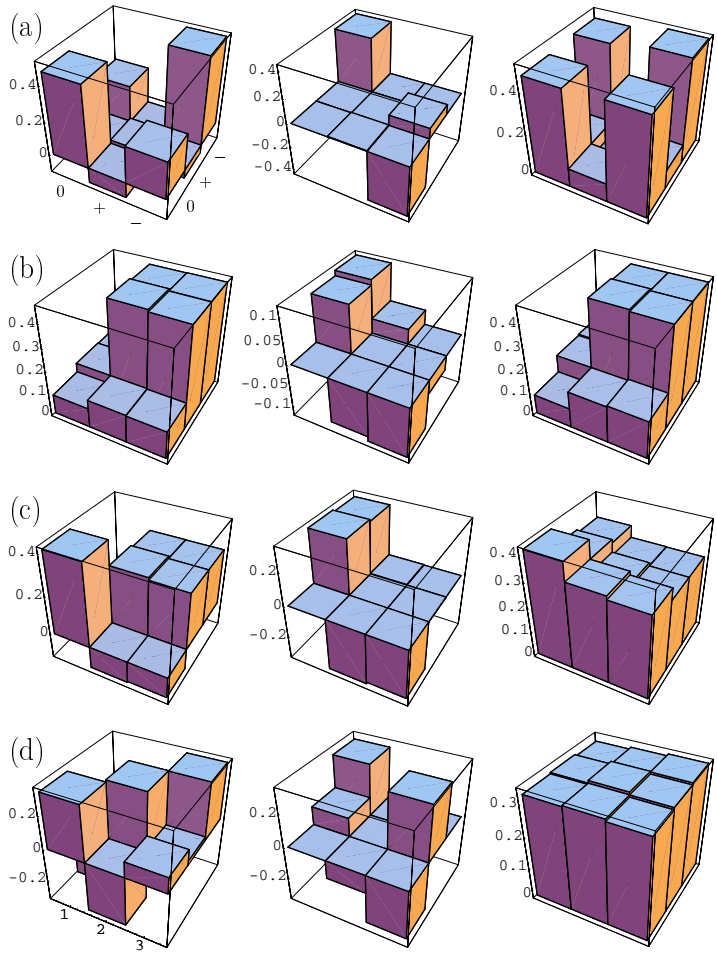

Fig. 10.17. Results of quantum state tomography applied to three different remotely prepared states of Bob's qutrits. Left and middle panels show real and imaginary parts of the reconstructed density matrices; right panels show the absolute values of those elements for getting picture of how large the contributions are of the three basic states.

to be used to remove the unwanted $|0\rangle$ contribution via destructive interference. Due to the greater complexity of this operation the acutually prepared state was found to still contain a small contribution of the $|0\rangle$ component. In cases (c) and (d) the goal was to prepare an equal-weight superpositions of all three basic "inner" states with different phases. The tomography reveals that we have come very close to achieving this goal. The $|0\rangle$ component of state (c) had only a slightly greater weight than the other two, while state (d) was almost perfect.

10.6 Maximum-Likelihood Quantum Homodyne Tomography

In the final section of this chapter we discuss applications of the likelihood maximization technique to quantum homodyne tomography. Homodyne characterization of a quantum state of an optical mode is based on multiple phase-sensitive measurements of its electric field. The field quantum noise statistics collected at various optical phases provide enough information to reconstruct the density matrix of the ensemble of interest.

Since its proposal [82] and first experimental implementation [83] in the early 1990s, quantum homodyne tomography has become a robust and versatile tool of quantum optics and has been applied in many different experimental settings. As any statistical method, it is suitable for combining with the likelihood maximization technique. Indeed, a homodyne measurement run yields a set of statistical data, whose likelihood with respect to a particular quantum ensemble can be evaluated easily. The goal of this section is to describe the way of finding the hypothetical ensemble which maximizes the probability of acquiring a particular data set. In writing this section we have assumed the reader to be familiar with the basics of quantum homodyne tomography; otherwise we recommend to refer to chapter by Raymer and Beck of this volume for a detailed review.

We consider a homodyne tomography experiment performed on an optical mode prepared repeatedly in the same quantum state $\hat{\rho}$. In an experimental run one measures the field quadrature at various phases of the local oscillator. Each measurement is associated with the observable $\hat{X}_\theta = \hat{X}\cos\theta + \hat{P}\sin\theta$, where $\hat{X}$ and $\hat{P}$ are the canonical position and momentum operators and θ is the local oscillator phase.

For a given phase θ, the probability to detect a particular quadrature value x is given by

$$\mathrm{pr}_\theta(x) = \mathrm{Tr}[\hat{\Pi}(\theta, x)\hat{\rho}], \tag{10.53}$$

where $\hat{\Pi}(\theta, x) = |\theta, x\rangle\langle\theta, x|$ is the projector onto this quadrature eigenstate. In the Fock (photon number state) basis, the projection operator is expressed as

$$\Pi_{mn}(\theta, x) = \langle m|\,\hat{\Pi}(\theta, x)\,|n\rangle = \langle m|\theta, x\rangle\,\langle\theta, x|n\rangle\,, \tag{10.54}$$

where the overlap between the number and quadrature eigenstates is given by the well known stationary solution of the Schrödinger equation for a particle in a harmonic potential:

$$\langle m|\theta, x\rangle = e^{im\theta}\left(\frac{2}{\pi}\right)^{1/4}\frac{H_n(x)}{\sqrt{n!}}\;\exp(-q^2), \tag{10.55}$$

with H_n denoting the Hermite polynomials[7].

[7] The additional phase factor $e^{im\theta}$ originates from the properties of the phase-space rotation operator [81] $\hat{U}(\theta) = e^{-i\theta\hat{n}}$. From $\hat{U}^\dagger(\theta)\hat{a}\hat{U}(\theta) = \hat{a}e^{-i\theta}$ we find for the

Consider an experimental run consisting of N field quadrature measurements at various local oscillator phases θ_i. For a given ensemble, the likelihood of obtaining a specific set of results $\{x_i\}$ is the product of individual probabilities (10.53) for each result

$$\ln \mathcal{L} = \sum_i \ln \mathrm{pr}_{\theta_i}(x_i). \tag{10.56}$$

We now solve the inverse problem of estimating the ensemble $\hat{\rho}$ that maximizes the likelihood of a given data set $\{\theta_i, x_i\}$ by means of the iterative algorithm described in chapter by Hradil *et al.*. We apply the iteration operator

$$\hat{R}(\hat{\rho}) = \sum_i \frac{\hat{\Pi}(\theta_i, x_i)}{\mathrm{pr}_{\theta_i}(x_i)}, \tag{10.57}$$

to the density matrix according to (3.40) of chapter by Hradil *et al.* so each step preserves the positivity of the density matrix:

$$\hat{\rho}^{k+1} = \mathcal{N}\left[\hat{R}(\hat{\rho}^k)\hat{\rho}^k\hat{R}(\hat{\rho}^k)\right], \tag{10.58}$$

where $\mathcal{N}$ denotes normalization to a unitary trace.

In practice, the iteration algorithm is executed in the photon number (Fock) representation. Since the Hilbert space of optical states is of infinite dimension, the implementation of the algorithm requires its truncation so the Fock terms above a certain threshold are excluded from the analysis. This assumption conforms to many practical experimental situations in which the intensities of fields involved are a priori limited.

We note that the scheme above does not involve evaluating marginal distributions, i.e. histograms of the quadrature data $\mathrm{pr}_\theta(x)$ associated with particular phases. Elimination of this intermediate step from the reconstruction scheme allows one to avoid approximating the phase and quadrature values and thus further enhance the accuracy of the method.

It is instructive to compare the maximum likelihood quantum state estimation with the traditional methods: reconstruction of the Wigner function by means of the inverse Radon transformation [81] and evaluation of the density matrix using quantum state sampling (see Raymer and Beck in this volume and [84, 85]). Figure 10.18 shows application of these two technique to the experimental data from [86]. The data set consists of 14152 quadrature samples of an ensemble approximating a coherent superposition of the single-photon and vacuum states.

The reconstruction shown in Fig. 10.18 reveals the advantages of the ML technique in comparison with the standard algorithm. First, the finite

quadrature operator $\hat{U}^\dagger(\theta)\hat{X}\hat{U}(\theta) = \hat{X}_\theta$ and for its eigenstate $|\theta, x\rangle = \hat{U}^\dagger|0, x\rangle$. From the first and last relations above, we obtain $\langle m|\theta, x\rangle = e^{i\theta m}\langle m|0, x\rangle$. The quantity $\langle m|0, x\rangle$ is the energy eigenwavefunction of a harmonic oscillator.

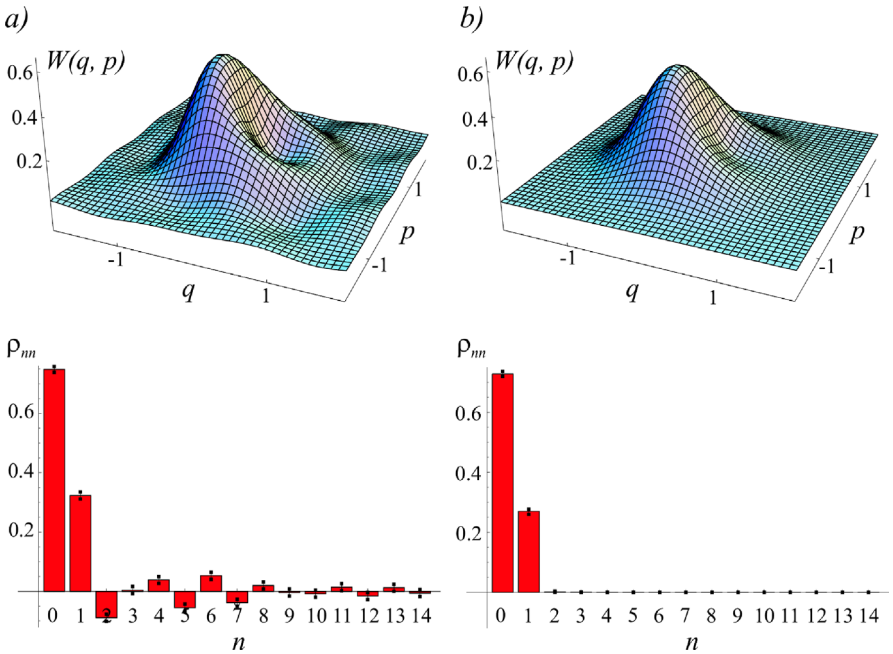

Fig. 10.18. Estimation of an optical ensemble from a set of 14152 experimental homodyne measurements [86] by means of the inverse Radon transformation (a) and the likelihood maximization algorithm (b). The Wigner function and the diagonal elements of the reconstructed density matrix are shown. The inverse Radon transformation in (a) was performed by means of the filtered back-projection algorithm with the cutoff frequency of 6.3. The statistical uncertainties in (b) were determined by means of a Monte-Carlo simulation (see text).

amount and discrete character of the data available leads necessarily to statistical noise which prevents one from extracting complete information about a quantum state of infinite dimension. To deal with this issue, both techniques apply certain assumptions on the ensemble to be reconstructed. While the ML algorithm truncates the Fock space, the filtered back-projection imposes low pass filtering to the Fourier image of the Wigner function[8], i.e. assumes the ensemble to possess a certain amount of "classicality" [82]. The latter assumption is dictated by mathematical convenience and is much less physically founded than the former. The ripples visible in the Wigner function reconstruction in Fig. 10.18(a) are a direct consequence of statistical noise and are associated with the unphysical high number terms in the density matrix. Such ripples are typical of the inverse Radon transformation [88].

[8] The pattern function reconstruction of the density matrix is free form this drawback as it does not involve spectral filtering and relies on truncating the Fock space instead.

Second, the back-projection algorithm does not impose any a priori restrictions on the reconstructed ensemble. This may lead to unphysical features in the latter, such as negative diagonal elements of the density matrix in Fig. 10.18(a). The ML technique, on the other hand, allows to incorporate the positivity and unity-trace constraints into the reconstruction procedure, thus always yielding a physically plausible ensemble [89, 90].

A third important advantage of the ML technique is the possibility to incorporate the detector inefficiences. In a practical experiment, the photodiodes in the homodyne detector are not 100% efficient, i.e. they do not transform every incident photon into a photoelectron. This leads to a distortion of the quadrature noise behavior which needs to be adjusted for in the reconstructed ensemble.

A common model for an homodyne detector of non-unitary efficiency η is a perfect detector preceded by a fictitious beam splitter of transmission η. The reflected mode is lost so the transmitted density matrix undergoes a so-called generalized Bernoulli transformation [81]:

$$\langle m|\,\hat{\rho}_\eta\,|n\rangle = \sum_{k=0}^{\infty} B_{m+k,m}(\eta)B_{n+k,n}(\eta)\,\langle m+k|\,\hat{\rho}_0\,|n+k\rangle\,, \tag{10.59}$$

where $\hat{\rho}_0$ and $\hat{\rho}_\eta$ are the density matrices of the original and transmitted ensembles, respectively, and $B_{n+k,n} = \sqrt{\binom{n+k}{n}\eta^n(1-\eta)^k}$. Under these circumstances the probability (10.53) of detecting a quadrature value x becomes

$$\begin{aligned}\mathrm{pr}_\theta^\eta(x) &= \langle\theta,x|\,\hat{\rho}_\eta\,|\theta,x\rangle \qquad (10.60)\\ &= \sum_{m,n=0}^{\infty}\sum_{k=0}^{\infty} B_{m+k,m}(\eta)B_{n+k,n}(\eta)\,\langle n|\theta,x\rangle\,\langle\theta,x|m\rangle\,\langle m+k|\,\hat{\rho}_0\,|n+k\rangle\,,\end{aligned}$$

so the projection operator $\hat{\Pi}(\theta,x)$ becomes replaced by a POVM element given by [91]

$$\hat{E}_\eta(\theta,x) = \sum_{m,n,k} B_{m+k,m}(\eta)B_{n+k,n}(\eta)\,\langle n|\theta,x\rangle\,\langle\theta,x|m\rangle\,|n+k\rangle\,\langle m+k|\,. \tag{10.61}$$

Aware of the homodyne detector efficiency η, one runs the iterative algorithm (10.57, 10.58) and reconstructs the original density matrix $\hat{\rho}_0$.

The performance of this technique is illustrated by Fig. 10.19 showing the reconstructed photon statistics of a coherent state measured with an inefficient detector. The estimated photon number distribution represents correctly the original state, in contrast to that obtained via the quantum state sampling followed by the inverted Bernoulli transformation [92].

Banaszek [93] has proposed an elegant modification of the ML state estimation method, applicable specifically to the evaluation of the Wigner functions. First, we notice that the Wigner function in the *origin* of the phase space can be determined using the diagonal elements of the density matrix

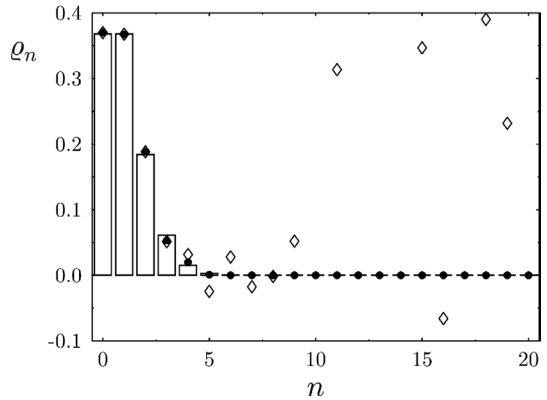

Fig. 10.19. (courtesy K. Banaszek, Oxford) Loss corrected reconstruction of the photon number distribution of an $\alpha = 1$ coherent state from 10^5 simulated homodyne data samples with the detector quantum efficiency $\eta = 0.85$. Filled circles represent the maximum likelihood estimation, hollow diamonds represent the quantum state sampling reconstruction followed by an inverse Bernoulli transformation.

in the Fock basis [94]:

$$W(0,0) = \sum_{n=0}^{\infty} (-1)^n \rho_{nn}. \tag{10.62}$$

These elements can be evaluated by means of the ML algorithm, simplified in the following manner. Since we are interested only in the diagonal elements of the density matrix, we set all off-diagonal elements of $\hat{\rho}$ to zero. This new diagonal density matrix $\hat{\rho}'$ corresponds to a optical ensemble which is symmetric with respect to phase rotations. The phase-sensitive off-diagonal elements of the projection operator (10.54) can therefore be neglected. Furthermore, the iteration step (10.58) can be reduced to $\hat{\rho}^{k+1} = \mathcal{N}\left[\hat{R}(\hat{\rho}'^n)\hat{\rho}'^n\right]$ with no risk of arriving at a nonpositive density matrix.

Repetitive application of the iteration above reconstructs the photon distribution and the value of the Wigner function at the phase space origin. To evaluate the Wigner function $W(p,q)$ at any *arbitrary* point, one applies the phase space displacement $\hat{D}(-p,-q)$ to the ensemble $\hat{\rho}$ so the point (p,q) gets transferred to the origin. In terms of the quadrature data, this corresponds to the shift

$$x_i \to x_i - q\cos\theta_i - p\sin\theta_i. \tag{10.63}$$

Upon this transformation, we apply the iterative algorithm again and calculate the Wigner function at the desired phase space location.

This scheme may appear more involved than the one discussed in the beginning of the section, as one needs to run a separate iteration series for

every point in which the Wigner function is to be calculated. However, due to a smaller number of parameters and a simplified iteration step, each iteration takes less time and the series converges faster. The choice of a particular scheme depends on a specific task and on the chosen truncation threshold in the Fock space.

Finally, we address the issue of statistical errors in ML homodyne tomography. Hradil *et al.* in this volume described the way of estimating the error by diagonalizing the Fisher information matrix. Although this method is generally applicable here, it does not regard the density matrix positivity constraint. If one of the parameters lies near the boundary of the positivity region, the statistical error will be governed by the first rather than the second derivative of the likelihood, and the actual uncertainty will be smaller than the one estimated.

A sensible alternative is offered by a clumsy, yet simple and robust technique of *simulating* the quadrature data that would be associated with the estimated ensemble $\hat{\rho}_{ML}$ if it were the true state. One generates a large number of random sets of homodyne data according to (10.53), then applies the ML reconstruction scheme to each set and obtains a series of density matrices $\hat{\rho}'_i$ each of which approximates the original matrix $\hat{\rho}_{ML}$. The average difference $\langle|\hat{\rho}_{ML} - \hat{\rho}'_i|\rangle_i$ evaluates the statistical uncertainty associated with the reconstructed density matrix.

Conclusion

The goal of this chapter was two-fold. First of all, considering several different experimental setups, the general principles of ML estimation discussed in chapter by Hradil *et al.* were shown "at work." The second goal was to compare the outcomes of ML estimation to that of other, more standardly used, reconstruction techniques. In all discussed cases, the ML estimation was seen to provide better results. We hope we persuaded the reader that the ML estimation is a versatile and highly efficient tool that can be applied to almost any reconstruction problem. We also believe that especially in quantum theory, where the experiments are often very demanding, the high efficiency of ML estimation is worth of somewhat larger computing costs compared to standard techniques. The aim of our research could be paraphrased as our credo: *If the experiment deserves to be done, then the data certainly deserve to be treated properly.* Anybody familiar with the rules of logic would agree that this statement could also be rephrased as the negative affirmation: *If the data are not treated properly, the experiment did not deserve to be done.*

Acknowledgments

The authors would like to acknowledge support by the following grants and projects. J. Řeháček and Z. Hradil: Grant No. LN00A015 of the Czech Min-

istry of Education and East-West program of the Austrian Academy of Sciences; G. Badurek, H. Rauch, and M. Zawisky: Project No P14229-PHY of the Austrian Science Foundation and Böhler Bleche GmbH, Mürzzuschlag, Austria; G. Molina-Terriza: Marie Curie Fellowship, project number SFB 015 P06 of Austrian Science Foundation (FWF), and contract No. IST-2001-38864, RAMBOQ of the European Commission; A. I. Lvovsky: Emmy Noether research grant of the Deutsche Forschungsgemeinschaft.

References

1. M. M. Nieto: Phys. Scr. T **48**, 5 (1993).
2. A. Royer: Phys. Rev. A **53**, 70 (1996).
3. R. Lynch: Phys. Reports **256**, (1995).
4. V. Peřinová and A. Lukš: *Phase in Optics* (World Scientific, Singapore, 1998).
5. A. Luis and L. L. Sánchez-Soto: In *Progress in Optics*, vol 41, ed by E. Wolf (Elsevier, Amsterdam, 2000).
6. C. W. Helstrom: *Quantum Detection and Estimation Theory* (Academic Press, New York, 1976).
7. B. Yurke, S. L. McCall, and J. R. Klaude: Phys. Rev. A **33**, 4033 (1986).
8. A. S. Lane, S. L. Braunstein, and C. M. Caves: Phys. Rev. A **47**, 1667 (1993).
9. M. J. Holland and K. Burnett: Phys. Rev. Lett. **71**, 1355 (1993).
10. B. C. Sanders and G. J. Milburn: Phys. Rev. Lett. **75**, 2944 (1995).
11. A. V. Chizhov, V. De-Renzi, and M. G. A. Paris: Phys. Lett. A **237**, 201 (1998).
12. L. Susskind and J. Glogower: Physics **1**, 49 (1964).
13. S. M. Barnett and D. T. Pegg: Phys. Rev. Lett. **76**, 4148 (1996).
14. Z. Hradil: Phys. Rev. A **55**, R1561 (1997).
15. M. G. Kendall and A. Stuart: *Advanced Theory of Statistics*, vol 2 (Charles Griffin, London, 1961).
16. K. R. W. Jones: Annals of Phys. **207**, 140 (1991).
17. Z. Hradil et al: Phys. Rev. Lett. **76**, 4295 (1996).
18. M. Zawisky et al: J. Phys. A: Math. Gen. **31**, 551 (1998).
19. J. Řeháček, Z. Hradil, M. Zawisky, S. Pascazio, H. Rauch, and J. Peřina: Phys. Rev. A **60**, 473 (1999).
20. J. Řeháček, Z. Hradil, M. Dušek, O. Haderka, and M. Hendrych: J. Opt. B: Quantum Semiclass. Opt. **2**, 237 (2000).
21. J. W. Noh, A. Fougères, and L. Mandel: Phys. Rev. Lett. **67**, 1426 (1991).
22. J. W. Noh, A. Fougères, and L. Mandel: Phys. Rev. Lett. **71**, 2579 (1993).
23. J. F. Walkup and J. W. Goodman: J. Opt. Soc. Am. **63**, 399 (1973).
24. A.C. Kak, and M. Slaney: *Principles of Computerized Tomographic Imaging*, ed by R.F. Cotellessa (IEEE Press, 1987).
25. B. Schillinger, W. Blümlhuber, A. Fent, and M. Wegner: Nucl. Instr. and Methods, **A424**, 58 (1998).
26. B. Schillinger, E. Lehmann, and P. Vontobel: Physica B **276**, 59 (2000).
27. S. Koerner, B. Schillinger, P. Vontobel, and H. Rauch: Nucl. Instrum. Meth. A **471**, 69 (2001).
28. P.J. McMahon, B.E. Allman, K.A. Nugent, D.L. Jacobson, M. Arif, and S.A. Werner: Appl. Phys. Lett. **78**, 1011 (2001).

29. F. Dubus, U. Bonse, T. Biermann, M. Baron, F. Beckmann, and M. Zawisky: SPIE Proc. **4503**, 259 (2002).
30. M. Zawisky, M. Bastürk, J. Řeháček, Z. Hradil: J. Nucl. Mater. **327**, 188 (2004).
31. W. Treimer, P. Maaß, H. Strothmann, and U. Feye-Treimer: Physica B **17**, 532 (1991).
32. P. Maaß, W. Treimer, and U. Feye-Treimer: Impact of Computing in Science and Engineering **4**, 250 (1992).
33. W. Treimer and U. Feye-Treimer: Physica B **241**, 1228 (1998).
34. B.E. Allman, P.J. McMahon, K.A. Nugent, D. Paganin, D.L. Jacobson, M. Arif, and S.A. Werner: Nature **408**, 158 (2000).
35. U. Bonse, R. Nusshardt, F. Busch, R. Pahl, J.H. Kinney, Q.C. Johnson, R.A. Saroyan, M.C. Nichols: Journal of Materials Science **26**, 4076 (1991).
36. V.F. Sears: *Neutron Optics*, (Oxford University Press, Oxford, 1989).
37. S. Quabis, R. Dorn, M. Eberler, O. Glöckl, and G. Leuchs: Appl. Phys. B **72**, 109 (2001)
38. J. Řeháček, Z. Hradil, O. Haderka, J. Peřina Jr., and M. Hamar: Phys. Rev. A, **67**, 061801 (2003).
39. U. Janicke and M. Wilkens: J. Mod. Optics **42**, 2183 (1995).
40. A.P. Dempster, N.M. Laird, and D.B. Rubin: J. R. Statist. Soc. B **39**, 1 (1977).
41. Y. Vardi and D. Lee: J. R. Statist. Soc. B **55**, 569 (1993).
42. L.A. Shepp and Y. Vardi: IEEE Trans. Med. Imag. **1**, 113 (1982).
43. Y. Vardi, L.A. Shepp, and L. Kaufman: Statist. Assoc. **80**, 8 (1985).
44. B.A. Mair, M. Rao, and J.M.M. Anderson: Inverse Problems **12**, 965 (1996).
45. H. Rauch, J. Summhammer, M. Zawisky, and E. Jericha: Phys. Rev. A **42**, 3726 (1990).
46. J. Řeháček, Z. Hradil, M. Zawisky, W. Treimer, and M. Strobl: Europhysics Letters **59**, 694 (2002).
47. V.F. Sears: Neutron News, **3**, 26 (1992).
48. S. Koerner, B. Schillinger, P. Vontobel, and H. Rauch: Nucl. Instrum. Meth. A **471**, 69 (2001).
49. F. Dubus, U. Bonse, M. Zawisky, M. Baron, and R. Loidl: *First Phase-Contrast Tomography with thermal neutrons*, 7^{th} World Conference on Neutron Radiography, Roma (2002), European Commission Special Book, in print; IEEE Transactions of Nuclear Science, Special Issue, in print.
50. A. Momose: Nucl. Instr. and Methods A **352**, 622 (1995).
51. A. Momose, T. Takeda, Y. Itai, and K. Hirano: Nature Med **2**, 473 (1996).
52. F. Beckmann, U. Bonse, F. Busch, and O. Günnewig: J. Comput. Assist. Tomogr. **21**, 539 (1997).
53. G. Badurek, R.J. Buchelt, and H. Leeb: Physica B **276**, 588 (2000).
54. H. Rauch and S.A. Werner: *Neutron Interferometry* (Oxford University Press, Oxford, 2000).
55. M. Zawisky, H. Rauch, and Y. Hasegawa: Phys. Rev. A **50** 5000 (1994).
56. Z. Hradil, J. Summhammer, G. Badurek, and H. Rauch: Phys. Rev. A **62** 014101 (2000).
57. M. Bourennane, A. Karlsson, and G. Björk: Phys. Rev. A **64**, 012306 (2001).
58. H. Bechmann-Pasquinucci and A. Peres: Phys. Rev. Lett. **85**, 3313 (2000).
59. H. Bechmann-Pasquinucci and W. Tittel: Phys. Rev. A **61**, 62308 (2000).
60. D. P. DiVincenzo, T. Mor, P. W. Shor, J. A. Smolin, and B. M. Terhal: Commun. Math. Phys. **238**, 379 (2003).

61. S. D. Bartlett, H. de Guise, and B. C. Sanders: Phys. Rev. A **65**, 052316 (2002).
62. V. Karimipour, A. Bahraminasab, and S. Bagherinezhad: Phys. Rev. A **65**, 052331 (2002).
63. Andris Ambainis: Proceedings of STOC, 2001, pp 134–142.
64. C. Brukner, M. Zukowski and A. Zeilinger: Phys. Rev. Lett. **89**, 197901 (2002).
65. R. Jozsa, and J. Schlienz: Phys. Rev. A **62**, 012301 (2000).
66. H. de Riedmatten, I. Marcikic, H. Zbinden and N. Gisin: Quantum Information and Computation **2**, 425 (2002).
67. M. Zukowski, A. Zeilinger, M. A. Horne: Phys. Rev. A **55**, 2564 (1997).
68. A. Mair, A. Vaziri, G. Weihs, and A. Zeilinger: Nature **412**, 313 (2001).
69. A. Vaziri, J. W. Pan, T. Jennewein, G. Weihs and A. Zeilinger: Phys. Rev. Lett. **91**, 227902 (2003).
70. A. Vaziri, G. Weihs and A. Zeilinger: Phys. Rev. Lett. **89**, 240401 (2002).
71. G. Molina-Terriza, J. P. Torres and L. Torner: Phys. Rev. Lett. **88**, 013601 (2002).
72. A. Vaziri, G. Weihs, and A. Zeilinger: J. Opt. B: Quantum Semiclass. **4**, S47 (2002).
73. J. P. Torres, Y. Deyanova, L. Torner and G. Molina-Terriza: Phys. Rev. A **67**, 052313 (2003).
74. J. P. Torres, A. Alexandrescu and L. Torner: Phys. Rev. A **68**, 050301 (2003).
75. L. Allen, M. W. Beijersbergen, R. J. C. Spreeuw, and J. P. Woerdman: Phys. Rev. A **45**, 8185 (1992).
76. H. He, M.E. Friese, N.R. Heckenberg, and H. Rubinsztein-Dunlop: Phys. Rev. Lett. **75**, 826 (1995).
77. M. E. J. Friese, J. Enger, H. Rubinsztein-Dunlop, and N.R. Heckenberg: Phys. Rev. A **54**, 1593 (1996).
78. V. Yu Bazhenov, M. V. Vasnetsov, and M. S. Soskin: JETP Lett. **52** 429 (1990).
79. N. R. Heckenberg, R. McDu., C. P. Smith, and A. G. White: Opt. Lett. **17**, 221 (1992).
80. J. Řeháček, Z. Hradil, and M. Ježek: Phys. Rev. A **63**, 040303(R) (2001).
81. Ulf Leonhardt: *Measuring the Quantum State of Light* (Cambridge University Press, Cambridge, 1997).
82. K. Vogel and H. Risken, Phys. Rev. A **40**, 2847 (1989)
83. D. T. Smithey, M. Beck, M. G. Raymer, and A. Faridani, Phys. Rev. Lett. **70**, 1244 (1993);
84. G. M. D'Ariano, U. Leonhardt, H. Paul: Phys. Rev. A **52**, 1801(R) (1995).
85. U. Leonhardt, M. G. Raymer: Phys. Rev. Lett. **76**, 1985 (1996).
86. A. I. Lvovsky and J. Mlynek: Phys. Rev. Lett **88** 250401 (2002).
87. W. Vogel: Phys. Rev. Lett. **84**, 1849 (2000).
88. G. Breitenbach, S. Schiller, and J. Mlynek: Nature **387**, 471 (1997); H. Hansen et al: Opt. Lett. **26**, 1714 (2001).
89. K. Banaszek: Phys. Rev. A **57**, 5013 (1998).
90. K. Banaszek: Acta Phys. Slov. **48**, 185 (1998).
91. K. Banaszek et al: Phys. Rev. A **61**, 010304 (2000).
92. T. Kiss, U. Herzog, U. Leonhardt: Phys. Rev. A **52**, 2433 (1995).
93. K. Banaszek: Phys. Rev. A **59**, 4797 (1999).
94. A. Royer: Phys. Rev. A **15**, 449 (1977); B.-G. Englert: J. Phys. A **22**, 625 (1989); H. Moya-Cessa and P. L. Knight: Phys. Rev. A **48**, 2479 (1993).